ÇUKUROVA UNIVERSITY
INSTITUTE OF NATURAL AND APPLIED SCIENCES

PhD THESIS

Gül GÖKBULUT

MOMENTUM SCALE CALIBRATION OF MUON TRACKS USING THE MUON PAIRS FROM J/ψ DECAYS AND INSTALLATION AND COMMISSIONING WORK IN CMS AT CERN

DEPARTMENT OF PHYSICS

ADANA, 2014

ÇUKUROVA UNIVERSITY
INSTITUTE OF NATURAL AND APPLIED SCIENCES

MOMENTUM SCALE CALIBRATION OF MUON TRACKS USING THE MUON PAIRS FROM J/ψ DECAYS AND INSTALLATION AND COMMISSIONING WORK IN CMS AT CERN

Gül GÖKBULUT

PhD THESIS

DEPARTMENT OF PHYSICS

We certify that the thesis titled above was reviewed and approved for the award of degree of the Doctor of Philosophy by the board of jury on 06/06/2014.

………………………………   ……………………………...   …………………….......
Prof. Dr. Aysel Kayış TOPAKSU   Prof. Dr. Eda EŞKUT   Prof. Dr. Sefa ERTÜRK
SUPERVISOR   MEMBER   MEMBER

………………………….   …………………….......
Prof. Dr. Ayşe POLATÖZ   Doç. Dr. Kenan SÖĞÜT
MEMBER   MEMBER

This PhD Thesis is performed in the Department of Physics of Institude of Natural and Applied Sciences of Çukurova University.
Registration Number:

Prof. Dr. Mustafa GÖK
Director
Institute of Natural and Applied Sciences

ABSTRACT

PhD THESIS

MOMENTUM SCALE CALIBRATION OF MUON TRACKS USING THE MUON PAIRS FROM J/γ DECAYS AND INSTALLATION AND COMMISSIONING WORK IN CMS AT CERN

Gül GÖKBULUT

ÇUKUROVA UNIVERSITY
INSTITUTE OF NATURAL AND APPLIED SCIENCES
DEPARTMENT OF PHYSICS

This thesis presents a study of light emitting diode (LED) stability and energy reconstruction of the HB and HE sub detectors of the Hadronic Calorimeter (HCAL) of the CMS experiment at CERN LHC.

In CMS the momentum measurement of muon tracks is affected by systematic uncertainties, incorrect mapping of the detector material, mismodeling of the magnetic field and problems of the reconstruction algorithms used to fit the track trajectory. This thesis also presents a study to calibrate the muon track momenta and to determine with precision their resolution on full 2011 data sample of the CMS detector.

Key Words: HCAL, CMS, LHC, Musclefit

ÖZ

DOKTORA TEZİ

J/ψ BOZUNUMLARINDAN GELEN MÜON İZLERİNİN MOMENTUM SKALA KALİBRASYONU VE CERN'DEKİ CMS DETEKTÖRÜNDE YAPILAN KURULUM VE VERİ ALMAYA HAZIRLIK ÇALIŞMALARI

Gül GÖKBULUT

ÇUKUROVA ÜNİVERSİTESİ
FEN BİLİMLERİ ENSTİTÜSÜ
FİZİK ANABİLİM DALI

Bu tezde, CERN, LHC'de CMS deneyindeki Hadronik Kalorimetre'nin (HKAL) HB ve HE alt detektörlerinin ışık yayıcı diyod (LED) kararlılığı ve enerji yeniden yapılandırılması sonuçları sunulmuştur.

CMS'de müon izlerinin momentum ölçümleri, sistematik belirsizlikler, detektör malzemesinin tam doğru olmayan haritalanması, manyetik alanların yanlış modellenmesi ve iz yörüngelerini yeniden yapılandırmak için kullanılan algoritmalardaki problemler yüzünden etkilenmektedir. Bu tez aynı zamanda CMS detektöründen alınan 2011 verileriyle müon izlerinin momentumlarının kalibrasyonu ve kararlılıklarının hassasiyetle ölçümü konusunda bir çalışma sunmaktadır.

Anahtar Kelimeler: HKAL, CMS, BHÇ, MuscleFit

ACKNOWLEDGMENTS

CONTENTS   **PAGE**

LIST OF TABLES **PAGE**

LIST OF FIGURES **PAGE**

X

ABBREVIATIONS

ATLAS   : A Toroidal LHC Apparatus

CERN   : Conceil Europeenne pour la Recherche Nucleaire

CB   : Crystal Ball

CMS   : Compact Muon Solenoid

CSC   : Cathode Strip Chambers

DAQ   : Data AcQusition

DT   : Drift Tubes

EB   : Electromagnetic Barrel

ECAL   : Electromagnetic CALorimeter

EE   : Electromagnetic Endcap

GUT   : Grand Unified Theory

HB   : Hadronic Barrel

HCAL   : Hadronic CALorimeter

HE   : Hadronic Endcap

HF   : Hadronic Forward

HLT   : High Level Trigger

HPDs   : Hybrid Photo Diodes

LED   : Light Emitting Diodes

LEP   : Large Electron – Positron collider

LHC   : Large Hadron Collider

LHCb   : Large Hadron Collider beauty

MC   : Monte Carlo

MuScleFit : Muon Scale Fit

PS   : Proton Synchrotron

PSB   : Proton Synchrotron Booster

QCD   : Quantum Chromo Dynamics

QED   : Quantum Electro Dynamics

RECO   : ReConstracted

RMS   : Root Mean Square

RPC   : Resistive Plate Chambers

SM   : Standard Model

SPS   : Super Proton Synchrotron

SST   : Silicon Strip Tracker

TEC   : Tracker End Caps

TIB   : Tracker Inner Barrel

TID   : Tracker Inner Disks

TOB   : Tracker Outer Barrel

1. INTRODUCTION

For thousands of years people have thought about one basic question; "What is the matter made of ?". This question led them to the development of atomic theory in early 20th century through Thomson's discovery of the electron in 1890, Rutherford's discovery of atomic nucleus in 1911, Bohr's model of the atomic structure in 1913. This was followed by the understanding of the quantized atom after the discovery of quantum mechanics in 1920s. Neutron was discovered in early 1930s by the work of J. Chadwick, W. Bothe, H. Becker and Irene and Joliot Curie. Initially electrons, protons and neutrons were believed to be the only elementary particles. However, the observation of some mesons, that have a mass between electron and proton lead scientists to the idea that there is much more and they were experimentally observed first in cosmic rays and then in particle accelerators with the development of appropriate technologies after 1950. Many years of hard work led to the Standard Model (SM), which aims to explain the properties of the building blocks of matter and their interactions. However The SM falls short of being a complete theory due to some open questions related to gravity, dark matter, dark energy, neutrino masses, matter and antimatter asymmetry. It looks like it is the low energy approximation of a more complete theory which is valid at higher energies. Lots of research is going on to discover new physics beyond the SM.

High Energy Physics is the branch of this new era, which aims to understand the nature of space and time, the characteristics of the forces governing the interactions of matter and energy, and the origins of the properties of the subatomic particles and their interactions. Subatomic particles can't be observed using low energies. Therefore, to investigate the elementary particles and their interactions high energies are needed. To collide particles in high energies; particle colliders, to understand the properties of the particles; detectors are needed.

The Large Hadron Collider (LHC) is the world's largest and most powerful particle accelerator, based at the European particle physics laboratory CERN, near Geneva in Switzerland. The LHC gives the opportunity to reproduce the conditions that existed within a billionth of a second after Big Bang. Scientists recreate these

2

conditions by colliding beams of protons or lead ions at velocities approaching the speed of light.

The Compact Muon Solenoid (CMS) Detector is one of the two general purpose experiments on LHC (the other one is ATLAS - A Toroidal LHC ApparatuS) designed to search for Higgs boson which was the only unobserved particle predicted by SM until recently and also new physics beyond SM.

This thesis presents a study to calibrate the muon track momenta and to determine with precision their resolution using the MuScle Fit Analysis on full 2011 data sample of the CMS detector. Some installation and commissioning work done in the hadronic calorimeter sub-detector (HCAL) of CMS is also given. In Chapter 2, some theoretical background on relevant concepts will be given. Brief overviews of the LHC, CMS detector and HCAL are presented in Chapter 3. The installation and commissioning work done on HCAL is explained in Chapter 4 and MuScle Fit Analysis is covered in Chapter 5. Conclusion is given in Chapter 6.

2. RELEVANT IDEAS AND CONCEPTS

As can be seen from the name "Compact Muon Solenoid", muon detection is one of the CMS's most important tasks. Muons are charged particles that are just like electrons and positrons, but are 200 times heavier. We expect them to be produced in the decay of both Higgs boson and also of particles which are signatures of new physics.

In this section a short description of the SM will be given and some topics which involve di-muon decays like Higgs search and also some of the directions in which discoveries of new physics seem most probable will be indicated.

2.1. The Standard Model (SM) of Particle Physics

The theoretical and experimental work of thousands of physicists since the 1930s have resulted in a remarkable model for the fundamental structure of matter: everything in the universe is made from 24 basic building blocks called fundamental particles. They are interacting by four fundamental forces. SM has successfully explained almost all experimental results and predicted a wide variety of phenomena. Over time and through many experiments, the Standard Model has become well established.

2.1.1. Fundamental Particles

All matter around us is made of elementary particles, the building blocks of matter. These particles occur in two basic types called quarks and leptons. Each
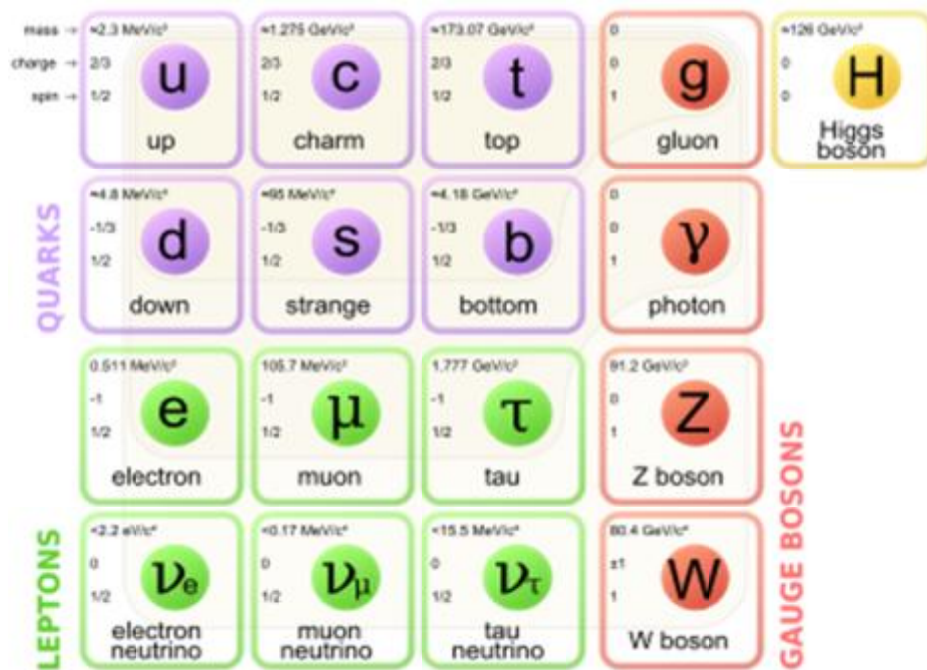
Figure 2.1. The particle content of Standard Model; fundamental particles, force carrier intermediate vector bosons and Higgs boson (http://en.wikipedia.org/wiki/Quark#mediaviewer/File:Standard_Model_ of_Elementary_Particles.svg)

group consists of six particles, which come in pairs in three "generations" (Figure 2.1). The lightest ones make up the first generation and they are the most stable. The particles in the second and third generations are heavier and less stable. All stable matter in the universe is made from particles in the first generation. Heavier particles quickly decay to the next most stable level. The quarks of the first generation are the "up quark" and the "down quark". "Charm quark" and "strange quark" belong to the second generation and "top quark" and "bottom (or beauty) quark" are in the third generation. Quarks also come in three different "colors"; red, blue and green and only mix in such ways as to form colourless objects. The six leptons are similarly arranged in three generations – the "electron" and the "electron neutrino", the "muon" and the "muon neutrino", and the "tau" and the "tau neutrino". The electron, the muon and the tau are massive particles which have an electric charge, whereas the neutrinos are electrically neutral and have very little mass.

The difference between the quarks and leptons is that whereas the quarks interact through electromagnetic, weak and strong interactions, leptons do not get

involved in strong interactions.

Each fundamental particle has a corresponding antiparticle. For charged particles the electrical charge of the antiparticle carries the opposite sign of that of the particle. For neutrinos and antineutrinos which are electrically neutral, the sign of the helicity is opposite. Neutrinos have left-handed helicities (spins antiparallel to momenta) and antineutrinos have right-handed helicities (spins parallel to momenta).

All the fundamental particles which build the matter have spin ½, therefore they are fermions.

2.1.2. Fundamental Forces and Carrier Particles

There are four fundamental forces in nature: the strong force, the weak force, the electromagnetic force, and the gravitational force. These forces have different ranges and different strengths. Gravity is the weakest force but its range is infinite. The electromagnetic force also has infinite range but it is much stronger than gravity. The weak and strong forces have a very short range and are effective only at the level of subatomic particles. The weak force is much stronger than gravity but it is indeed the weakest of the other three. The strong force, is the strongest of all four fundamental interactions.

Three of these four fundamental forces result from the exchange of spin-1 force-carrier particles. They are called "intermediate vector bosons". Particles of matter interact by exchanging these bosons with each other. Each fundamental force has its own corresponding boson – the strong force is carried by the "gluon", the electromagnetic force is carried by the "photon", and the mediators of weak force are "W and Z bosons". Although not yet found, the corresponding force-carrying particle of gravity is called the "graviton". The Standard Model includes the electromagnetic, strong and weak forces and their carrier particles, and explains how these forces act on the matter particles. However, gravity which is the most familiar force in our everyday lives, is not part of the Standard Model; because fitting gravity into this framework has proved to be a difficult challenge. No one has managed to make the quantum theory which describes the micro world, and the general theory of relativity

which describes the macro world, mathematically compatible in the context of the Standard Model. However the effect of gravity can be neglected because of the very small masses of the fundamental particles.

The main properties of intermediate vector bosons can be summarized as follows:

Photons, mediate the electromagnetic interactions between electrically charged particles. The photon is massless, neutral and is well described by the theory of quantum electrodynamics (QED).

W^+, W^- and Z^0 intermediate vector bosons mediate the weak interactions between all quarks and leptons. They are massive, with the Z^0 being more massive (91.2 GeV/c^2) than the $W^\pm$ (80.4 GeV/c^2). The charged intermediate bosons $W^\pm$ exclusively act on left-handed particles and right-handed antiparticles only. Furthermore, since the $W^\pm$ carries an electric charge of +1 or −1 it couples also to the electromagnetic interaction. The electrically neutral Z^0 boson interacts with both left-handed particles and antiparticles. These three intermediate bosons along with the photons are grouped together, as collectively mediating the electroweak interaction.

The gluons mediate the strong interactions between quarks. They are massless and electrically neutral but they carry color charge. There are 8 of them that are labeled by a combination of color and anticolor charge (e.g. red–antigreen) they carry. Because the gluons have an effective color charge, they can also interact among themselves. The gluons and their interactions are described by the theory of quantum chromodynamics (QCD). A phenomenon called "color confinement" results in quarks being perpetually bound together forming colorless hadrons: baryons which consist of three quarks with three different colors or mesons which consist of a quark and an antiquark carrying a color and its anticolor respectively.

2.1.3. Gauge Symmetry of the Standard Model

Mathematically, Standard Model is a quantum field theory with the gauge symmetry SU(3) ´ SU(2) ´ U(1). Its fundamental objects are "quantum fields" which are defined at all points in spacetime. These fields are:

· the fermion field, ψ, representing the fundamental particles,

· the electroweak boson fields W_1, W_2, W_3 and B,

· the gluon field, G_a; and

· the Higgs field, ϕ.

The dynamics of the quantum state and the fundamental fields are determined by a Lagrangian density $\mathcal{L}$. Standard Model Lagrangian density can be found in particle physics textbooks.

The SM is also a gauge theory, which means there are degrees of freedom in the mathematical formalism which do not correspond to changes in the physical state or in other words the Lagrangian density is invariant under a continuous group of local transformations. The gauge group of the SM is SU(3) ´ SU(2) ´ U(1). U(1) acts on B and ϕ, SU(2) acts on W and ϕ, and SU(3) acts on G. The fermion field ψ also transforms under these symmetries, although all of them leave some parts of it unchanged.

The principle of local gauge invariance works very well for the strong and electromagnetic interactions but application to the weak interactions is problematic because gauge fields must be massless whereas bosons carrying the weak interaction are quite massive. Fortunately, theorists Robert Brout, François Englert and Peter Higgs proposed a mechanism which exploits spontaneous symmetry breaking to solve this problem (Englert and Brout, 1964), (Higgs, 1964). According to the Brout-Englert-Higgs mechanism, an invisible scalar field, now called the "Higgs field", pervades the universe with a non-zero value even in "vacuum" and when $W^{\pm}$ and Z^0 interact with this field they gain mass. Just after the Big Bang the symmetry was

perfect and the Higgs field was zero but as the universe expanded and cooled below a critical value the symmetry broke down and the Higgs field grew spontaneously and particles interacting with it acquired a mass. The mass of the particle depends on its degree of interaction with this field, the more the interaction the heavier is the particle. Particles like the photon that do not interact with the Higgs field remain massless. The quantum of the Higgs field is the Higgs boson.

All the fundamental particles and intermediate vector bosons carrying the EM, weak and strong interactions have been observed experimentally. Among the particles predicted by the SM it was only the scalar Higgs boson for which there was no experimental evidence until very recently, although it has been predicted 50 years ago and is being actively searched for since 1980s.

2.1.4. Higgs Boson Search

Like the other very heavy particles, top quark, Ws and Z, Higgs bosons decay to other particles almost instantly; therefore it is not possible to observe them directly. Since the SM predicts the decay modes and their probabilities precisely (Figure 2.2), the production and decay of Higgs boson can be shown by careful examination of decay products of particle collisions.
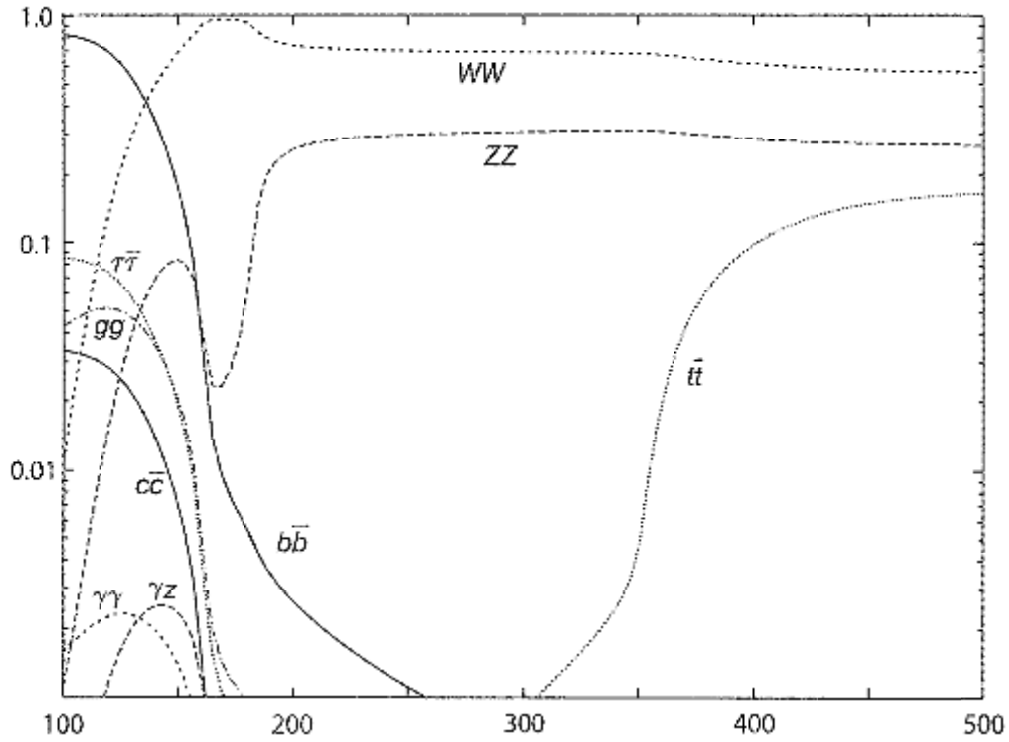
Figure 2.2. Branching ratios for Higgs decay, as functions of the Higgs mass (in GeV/c^2) (Gunion etal. , 1990)

The "golden" decay mode H ® ZZ ® 4μ process is one of the cleanest channels for discovering the SM Higgs boson at LHC.

The first extensive search for the Higgs boson was conducted at the Large Electron-Positron Collider (LEP) at CERN in the 1990s. When it stopped working in 2000, LEP had not found any conclusive evidence for the Higgs and set a lower bound for the Higgs boson of 114.4 GeV/c^2 at the 95% confidence level, with a small number of events around 115 GeV (YAO, 2006).

Data from CDF and DØ (Fermilab, Tevatron) experiments excluded the Higgs boson in the range 158–175 GeV/c^2 at 95% CL (AALTONEN, 2010). In addition, there was a small excess of events possibly indicating a Higgs boson with a mass between 115 GeV/c^2 and 140 GeV/c^2 (The CDF Collaboration, the DØ Collaboration, the Tevatron New Physics, Higgs Working Group, 2012) .

On 4 July 2012, the ATLAS and CMS experiments announced they had each observed a new particle in the mass region around 126 GeV. This particle is consistent with the Higgs boson but it will take further work to determine whether or

not it is the Higgs boson predicted by the SM (ATLAS Collaboration, 2012), (CMS Collaboration, 2012). At March 2013, LHC presented preliminary new results which threw more light on the particle discovered in 2012 after analysing two and a half times more data than was available for the discovery announcement in July. They have found that the new particle is looking more and more like a Higgs boson, the particle linked to the mechanism that gives mass to elementary particles. However, whether this is the Higgs boson of the Standard Model, or the lightest of several bosons predicted in some theories beyond the Standard Model is still an open question. More data is needed to find the answer to this question.

2.2. Grand Unification

With the success of electroweak unification, attempts to include the strong interactions in a 'Grand Unified Theory' (GUT) that would identify the three fundamental forces as different manifestations of a single interaction. There are several proposed GUT candidates like SU(5), SO(10), SU(8), O(16), symplectic groups, E8, supersymmetry and several others. Many of the GUTs predict additional heavy neutral gauge bosons Z¢(Leike, 1999). Current lower mass limit is of the order of 600-900 GeV/c^2. The LHC offers the opportunity to search for Z¢bosons using the Z¢® m^+ + m^- channel in a mass range significantly larger than 1 TeV (CMS Collaboration, 2007).

2.3. Matter-Antimatter Symmetry

The Big Bang should have created equal amounts of matter and antimatter. But today there is far more matter than antimatter in the universe. Obviously there must be an interaction that violates the baryon and lepton number conservation. Also there must be CP violation i.e. some reaction i ® f whose rate is different from its CP conjugate $\tilde{\iota} \rightarrow \tilde{f}$, otherwise there would be no net change in baryon number. One

good system to investigate CP violation is the decays of B mesons and they involve di-muon decays of J/ψ s.

3. EXPERIMENTAL APPARATUS

3.1. Large Hadron Collider (LHC)

The world's largest proton-proton and lead ion collider LHC; is installed in a hundred meters underground tunnel with a diameter of 3.8 m which has before hosted the e^+e^- collider LEP (Large Electron Positron). LEP had many precision measurements including the observations of $W^{\pm}$ and Z^0 bosons. Accelerated electrons and positrons have large energy loss due to the synchrotron radiation. This radiated energy is proportional to $E^4/(Rm^4)$, where E is the electron energy, m is the mass of the accelerated electrons and R is the radius of the accelerator. To increase the center-of-mass energy; one needs to increase the mass of the accelerated particles. Rest mass of protons is about 2000 times greater than rest mass of electrons. Therefore the energy loss due to the synchrotron radiation for protons is decreased by a factor of $(2000)^4 \approx 10^{13}$ compared to electrons. Collision rate is also very important: To produce a sufficient number of rare processes, very high collision rates are needed. The collision rate is proportional to the instantaneous luminosity of the accelerator, given by:

$$L = f \ \frac{n_1 n_2}{4\pi\sigma_x\sigma_y} \tag{3.1}$$

where f is the frequency, n_1 and n_2 are the number of particles per bunches, σ_x and σ_y are the transverse profile of the beam along x and y axes. The integrated luminosity is defined as:

$$L_{\text{int}} = \int L dt \tag{3.2}$$

Protons are injected into both of the LHC beam lines in contrast with the Tevatron accelerator at Fermilab which used proton–antiproton collisions. Tevatron was the highest energy collider before LHC. It worked from 1992 until 1998 with an

energy of 1.8 TeV, and between 2001 and 2011 with 1.96 TeV. The LHC operated at 3.5 TeV per beam in 2010 and 2011 and at 4 TeV in 2012. It shutdown for upgrades to increase the beam energy to 6.5 TeV per beam at the end of 2012, with reopening planned for early 2015. Using proton-proton collisions instead of proton-antiproton collisions is expected to increase the luminosity (L) by two orders of magnitude. The design luminosity of the LHC is $10^{34}cm^{-2}s^{-1}$ but during the first LHC run between 2010-2012 this value was not reached. The peak luminosity was 2.1 ´ $10^{32}cm^{-2}s^{-1}$ during 2010, 3.7 ´ $10^{33}cm^{-2}s^{-1}$ during 2011 and 7.7 ´ $10^{33}cm^{-2}s^{-1}$ during 2012.

The proton source of LHC is a bottle of compressed hydrogen gas. With an electric field, hydrogen atoms are stripped from their electron, leaving behind a sample of pure protons. These protons are accelerated to the energy of 50 MeV in the Linac 2, the first accelerator in the chain. The beam is then injected into the Proton Synchrotron Booster (PSB). To maximize the intensity of the beam the packet is divided into four, one for each of the boosters rings. Recombining the packet from the four rings. The booster accelerates the protons to an energy of 1.4 GeV. It's then followed by the Proton Synchrotron (PS). The PS further accelerates the beam to an energy of 25 GeV. The packets of protons are then channeled to the Super Proton Synchrotron (SPS) where they are accelerated to 450 GeV. Finally the SPS injects the proton beams directly into the two beam pipes of the LHC. The beam in one pipe circulates clockwise while the beam in the other pipe circulates anticlockwise. Each beam is accelerated to their maximum energy of 4 TeV and then brought into the collision inside of the four detectors; A Toroidal LHC Apparatus (ATLAS), The Compact Muon Solenoid (CMS), A Large Ion Collider Experiment (ALICE) and Large Hadron Collider beauty (LHCb). LHC accelerator system can be seen from Figure 3.1.
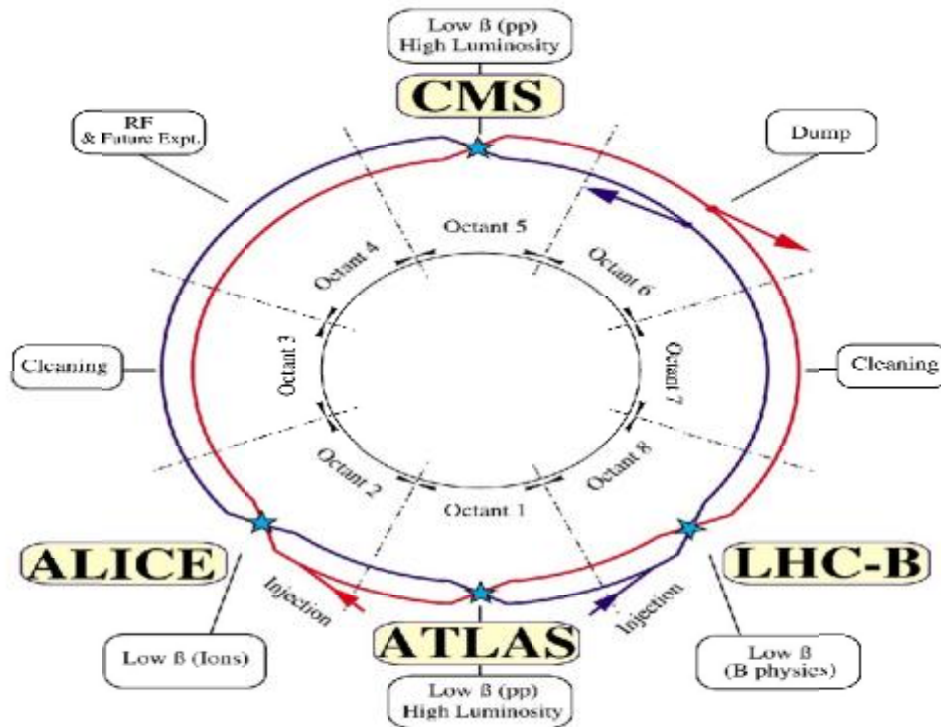
Figure 3.1. LHC accelerator system (http://www.lhc-closer.es/1/3/4/0)

ATLAS and CMS are general-purpose detectors that will detect the sub-particles released during collisions and investigate a wide range of physics. They are both searching for Higgs Boson, until recently the last unobserved fundamental particle in the SM physics but with different design and techniques. In addition to searching for new phenomena including supersymmetry, new massive vector bosons, extra dimensions etc. at the TeV scale physicists of CMS and ATLAS also aim to measure and understand deeply the previously discovered particles with unprecedented precision. ALICE is a heavy ion detector which is designed to study nucleus-nucleus interactions at LHC energies in order to observe the quark gluon plasma which is a highly energized form of matter that contains quarks and gluons. LHCb aims to understand the matter-antimatter asymmetry by studying the physics of b-quarks.

3.2. Compact Muon Solenoid

The Compact Muon Solenoid (CMS) is a general purpose detector which is located at interaction region 5 of the LHC. Sectional view of the CMS is shown in Figure 3.2.
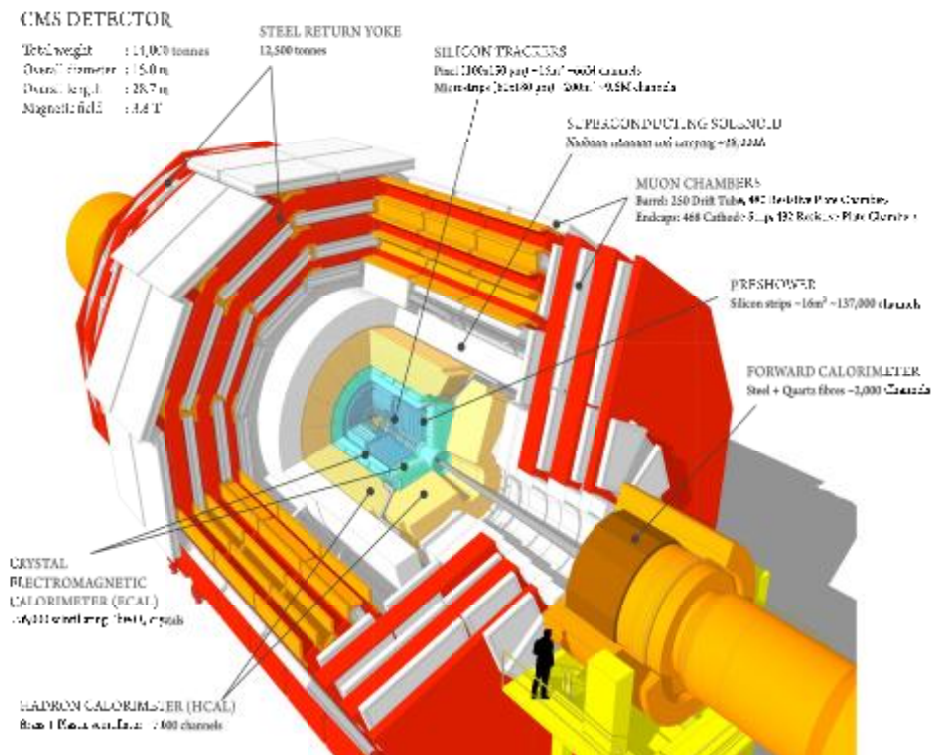
Figure 3.2. Sectional view of the CMS detector (http://cms.web.cern.ch/news/cms-detector-design)

The CMS has the largest superconducting solenoid ever built; A 13 meters long, 4T superconducting solenoid with a 5.9 meters inner diameter, sits at the heart of the CMS detector. CMS detector aims to identify muons, electrons, photons and jets in a wide energy range and to find new era physics by these accurate measurements. The CMS detector is designed to record and to reconstruct the proton proton collisions at $\sqrt{s}$=14 TeV center of mass energy with the luminosity of $L = 10^{34}$cm^{-2}s^{-1}.

There are different subsystems inside the magnet, which are: the silicon pixel detector, the silicon strip tracker, the electromagnetic calorimeter (ECAL), the HCAL and muon detectors.

More than 4300 scientists, engineers and support staff from 41 countries are working on the CMS experiment. The CMS experiment is one of the largest international scientific collaborations in the world.

3.2.1. Coordinate System of the CMS

The origin of the reference frame of the CMS detector is the particle collision point. The *y*-axis points vertically upward, *x*-axis points to the center of the LHC ring radially and the *z*-axis is in the direction of the beam. The azimuthal angle ϕ is measured from the *x*-axis in the *xy* plane and the radial coordinate in this plane is labeled by *r*. The polar angle θ is defined in the *rz* plane. The pseudorapidity is defined as $\eta = -\ln[\tan(\phi/2)]$.

The transverse momentum and the transverse energy which are measured perpendicular the beam direction are denoted respectively by p_T and E_T. Transverse momentum (p_T) is computed by the *x* and *y* components. The transverse energy on the other hand is computed by $E_T = E \sin\theta$.

3.2.2. The Tracker System

A silicon tracking system is installed in the center of CMS with a diameter of 3.5 m and length of 5.8 m, which is designed to reconstruct charged tracks and provide a precise measurement of the trajectories of charged particles as well as the precise reconstruction of the secondary vertices (CMS Collaboration, 2008).

Silicon tracking system consists of two parts: silicon strip tracker and the pixel detector.

3.2.2.1. Silicon Strip Tracker

Silicon Strip Tracker (SST) is divided into four subsystems; Tracker Inner Barrel (TIB), Tracker Outer Barrel (TOB), Tracker Inner Disks (TID) and Tracker End Caps (TEC) (see Figure 3.3.).
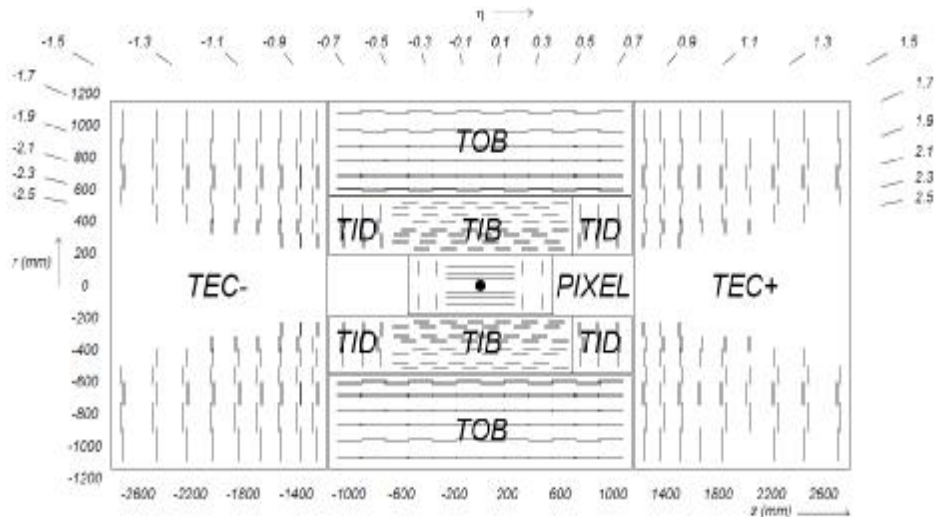
Figure 3.3. Schematic cross section through the CMS tracker. Each line represents a detector module. Double lines indicate back-to-back modules which deliver stereo hits (CMS Collaboration, 2008)

3.2.2.2. The Pixel Detector

The Pixel Detector is the part of the tracking system which is closest to the interaction region. It consists of three barrel layers (BPix) with two endcap disks (FPix) on each side of them. The BPix layers have a length of 53 cm and are located at mean radii of 4.4 cm, 7.3 cm and 10.2 cm. FPix disks are placed at $z = \pm 34.5$ and $z = \pm 46.5$. The pixel detector consists of 65 million pixels. Figure 3.4. shows the CMS pixel detector (CMS Collaboration, 2006).
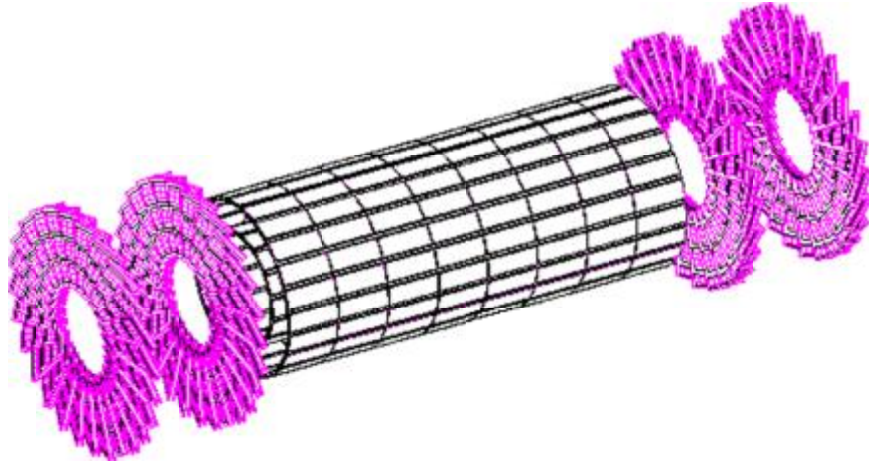
Figure 3.4. Layout of pixel detectors in the CMS tracker
            (http://www.hephy.at/user/friedl/diss/html/node27.html)

The tracker is used to reconstruct muons, electrons and charged hadrons, as well as to see tracks coming from the decay of very short-lived particles such as b-quark with high momentum and resolution efficiency. The tracker has an active silicon surface of about 200 m^2 which makes the CMS tracker the largest silicon tracker ever built.

In order to measure precisely the momenta of the muons in a wide kinematic range, the tracks from the tracker measurement are combined with the tracks from the outer muon system. The silicon tracker is exposed to a high level of radiation. Therefore the tracker is build to be radiation hard.

3.2.2.3. Vertex Reconstruction

The CMS detector is designed for full event reconstruction, including robust tracking and detailed vertex reconstruction using a full silicon tracker (CMS Collaboration, 2000). The reconstruction of interaction vertices is vital to reject tracks coming from pile-up events. The primary vertex is reconstructed in two steps. The reconstructed tracks which are thought to be coming from the vertex are considered at first. The z-coordinates of the points of the closest approach of these tracks to the beam (impact parameters) are calculated. The tracks with impact parameter smaller than 3 cm are kept. In the next step the vertices are reconstructed

using the kept tracks with a recursive method which estimates the parameters with a Kalman Filter algorithm (Speer, Prokofiev, Fruhwirth, Waltenberger and Vanlear, 2006). For a given event, the total transverse momentum of the associated tracks, Σp_T is used to order the primary vertices. The vertex reconstruction has a very good efficiency as can be seen from Figure 3.5. For muons the efficiency is about 99% for most of the pseudorapidity range.

Reconstruction of the secondary vertices is also possible by using tracks associated to jets and applying further selection cuts about the transverse impact parameter.
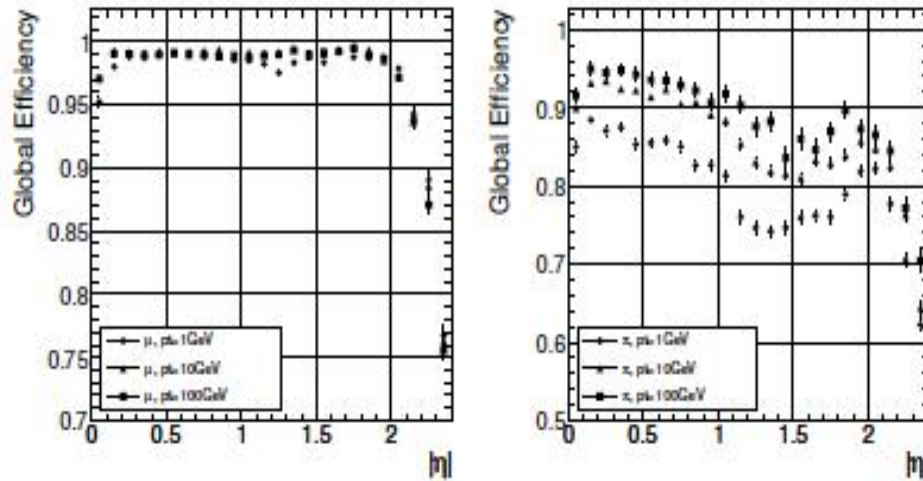
Figure 3.5. Global track reconstruction efficiency for muons (left panel) and pions (right panel) of transverse momenta of 1,10 and 100 GeV (CMS Collaboration, 2008)

3.2.3. Muon Spectrometer

Muons are the key signatures for many of the most interesting physics LHC is designed to explore. The muon system must fulfill some requirements in order to be able to detect these signatures and separate them from the background. The central concept of CMS, the Compact Muon Solenoid detector system is the ability to trigger on and reconstruct muons at the highest luminosities (The CMS Collaboration, 1997). Muons can traverse all the calorimeters without being stopped unlike other

particles. They can provide strong indication of interesting events which will be important for the new physics.

The following functionality and performance criteria are important to achieve the desired physics goals:

Muon Identification: At least 16 interaction lengths (present up to $\eta=2.4$) of material to allow a good muon identification by absorbing unwanted charged particles before (ECAL, HCAL) and inside the muon system (iron yoke).

Muon Trigger: Precise muon chambers are used together with fast dedicated trigger detectors to identify unambiguously beam crossing and trigger on single and multi-muon events with p_T thresholds from a few GeV to 100 GeV up to $\eta=3.1$.

Momentum Resolution: 8 to 15% $\delta p_T/p_T$ at 10 GeV and varies between 20% and 40% at 1 TeV for stand-alone momentum resolution, from 1.0 to 1.5% at 10 GeV and from 6 to 17% at 1 TeV after matching with the central tracker. For global momentum resolution, momentum-dependent spatial position matching at 1 TeV less than 1 mm in the bending plane and less than 10 mm in the non bending plane.

The muon system uses three types of gaseous detectors; drift tubes (DT), cathode strip chambers (CSC) and resistive plate chambers (RPC). Drift tubes are in the barrel covering the pseudorapidity region $|\eta| < 1.2$, while CSCs are in the endcap region covering $0.9 < |\eta| < 3.4$. DT and CSC detectors are used to measure the position of the tracks and provide precise measurement of the momentum of the muons. RPCs are trigger-dedicated muon detectors which deliver independent and fast trigger with high segmentation and sharp p_T threshold over a large part of the pseudorapidity range. They are located both in barrel and endcaps. CMS muon system is shown in Figure 3.6.
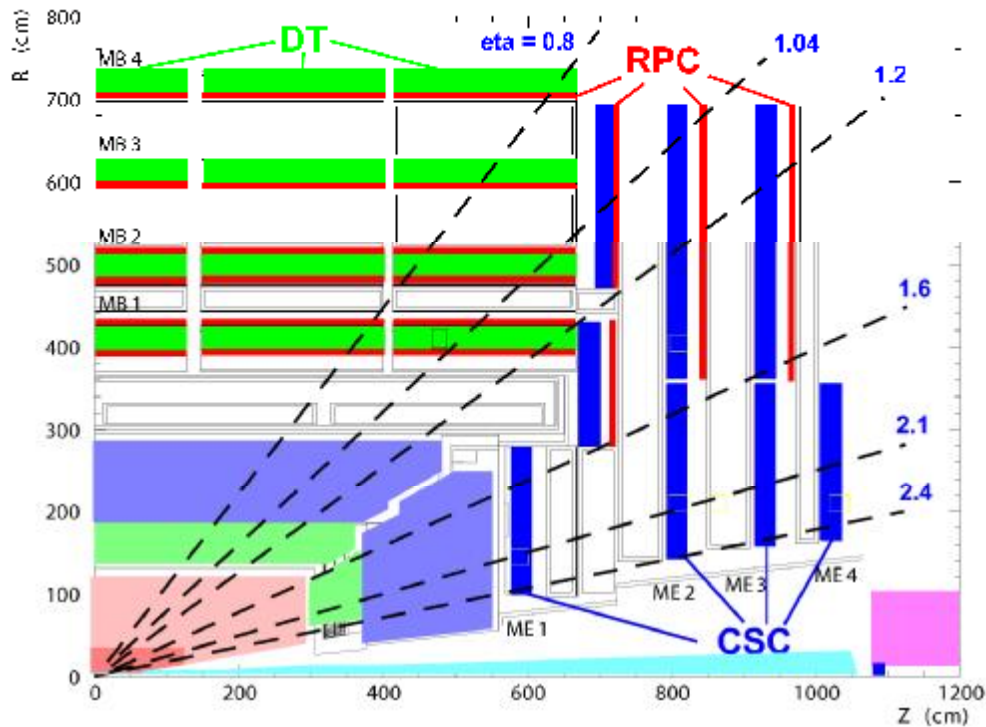
Figure 3.6. Muon system of the CMS. (Bontenackels, 2005)

3.2.3.1. Muon Reconstruction

Muon reconstruction is important not only for the discovery of new physics but also for precision measurements of SM processes. CMS detector is capable of detecting muons even if there is a high level of background, using together the muon system which provides an efficient identification of muons and the inner tracker which provides a very precise measurement of their properties. The muons can be reconstructed in three stages:

Local Reconstruction: It is the first step of the muon reconstruction. The raw data from the detector read-out (from DTs, CSCs and RPCs) are reconstructed as individual points in space.   Hits in each CSC and DT chambers are then matched to form track "segments" (track stubs).

Stand-alone Reconstruction: From the segments reconstructed in the muon chambers "seeds" are generated which consist of position and direction vectors and an estimate of the muon transverse momentum. Using these initial estimates as seeds, track fits are performed in the muon system, using segments and hits from

DTs, CSCs and RPCs and are based on the Kalman filter technique. The fitted tracks in the muon spectrometer are called **"stand-alone muons"**.

Global Reconstruction: In the last step stand-alone tracks are matched with tracker tracks to form global muons.

A schematic view of the steps of muon reconstruction is shown in Figure 3.7.
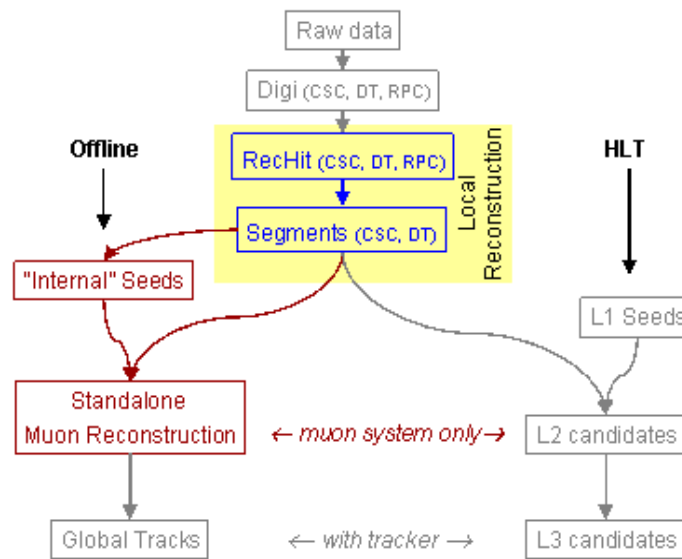
Figure 3.7. Steps of muon reconstruction
(https://twiki.cern.ch/twiki/bin/view/CMSPublic/SWGuideStandAloneMuonReco)

The reconstructed stand-alone, global and tracker muons are put together into a single software object. Further information like the energy collected in the matching calorimeter towers is also added into this object. In order to achieve a balance between efficiency and purity of the muon sample, this information can be used for further identification.

3.2.4. Calorimetry

Calorimetry is a powerful measurement method, which was developed for accelerator based particle physics experiments. It uses calorimeters as experimental apparatus. Calorimeters are blocks of instrumented material to measure the energy of particles. After entering the calorimeter most particles starts a particle shower, their energy gets fully absorbed and transformed into a measurable quantity. The CMS calorimeter system has two layers (Figure 3.8). The first layer is the ECAL. ECAL measures the electromagnetically interacting particles' energy. Second layer is the HCAL, which measures the energy of the strongly interacting particles.
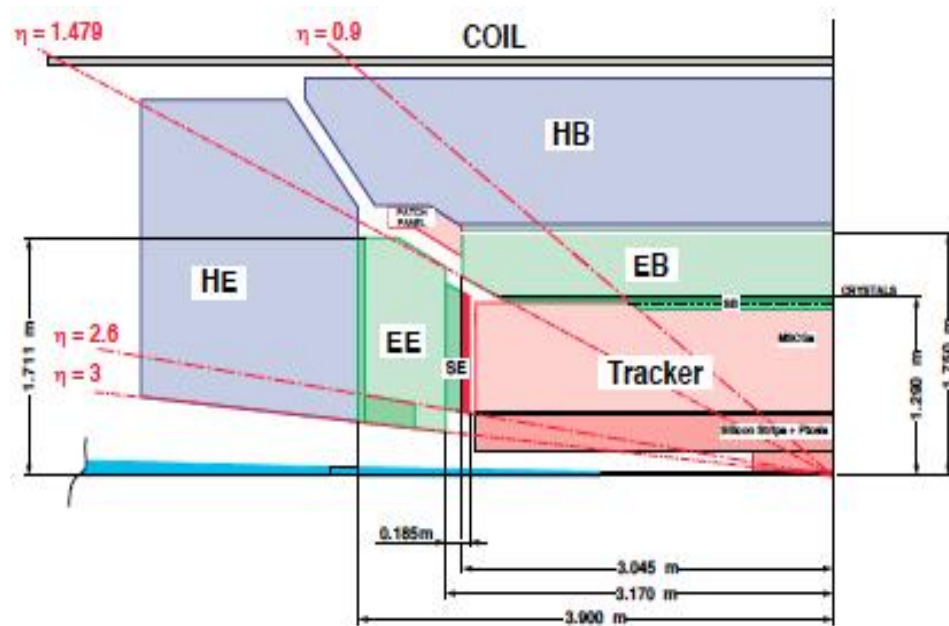
Figure 3.8. Schematic view of one quadrant of the calorimetry and tracking system
         (The CMS Collaboration 1997, The Electromagnetic Calorimeter
         Technical Design Report)

3.2.4.1. The Electromagnetic Calorimeter (ECAL)

The ECAL plays an essential role in the study of the physics of electroweak symmetry breaking, particularly through the exploration of the Higgs sector and is an important detector element for a large variety of SM and beyond SM physics

processes (The CMS Collaboration 1997, The Electromagnetic Calorimeter Technical Design Report).

The ECAL is made up of a barrel section and two endcaps and lays between the tracker and the HCAL. The electromagnetic barrel (EB) covers the region $|\eta| <$ 1.48 while the endcaps (EE) cover the region $1.5 < |\eta|$ 3.0 (see Fig 3.9). The preshower detector (ES) that sits in the endcaps provides extra spatial precision and helps distinguishing between single high-energy photons (signs of interesting physics) and the less interesting pairs of low energy photons close to each other. It covers $1.6 < |\eta| < 3.6$.
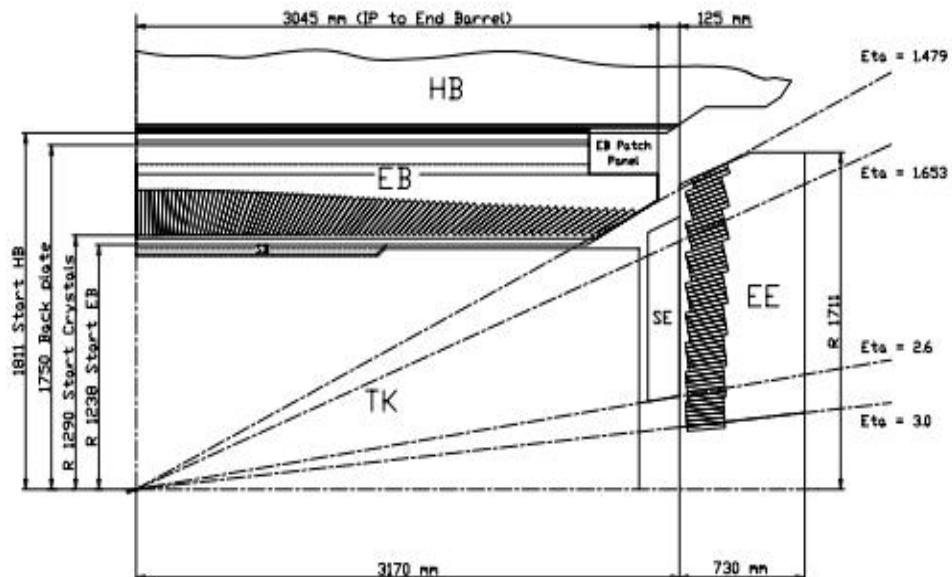
Figure 3.9. Longitudinal section of one quadrant of the ECAL (The CDF Collaboration, the D0 Collaboration, the Tevatron New Physics, Higgs Working Group, 2012)

3.2.4.2. The Hadronic Calorimeter (HCAL)

The HCAL surrounds the ECAL. HCAL together with ECAL is a complex calorimeter system for the measurement of the jets, quark and gluon directions and exotic particles resulting with apparent missing transverse energy. It also provides indirect measurement of the presence of non-interacting, uncharged particles such as neutrinos. The HCAL ranges from 1.77 m to 3.95 m in radial dimensions, covers the

pseudorapidity range |η| < 5.2 and consists of four sub-detectors: Hadronic Barrel (HB), Hadronic Endcap (HE), Hadronic Outer (HO) and Hadronic Forward (HF). A longitudinal view of CMS HCAL can be seen in Figure 3.10.
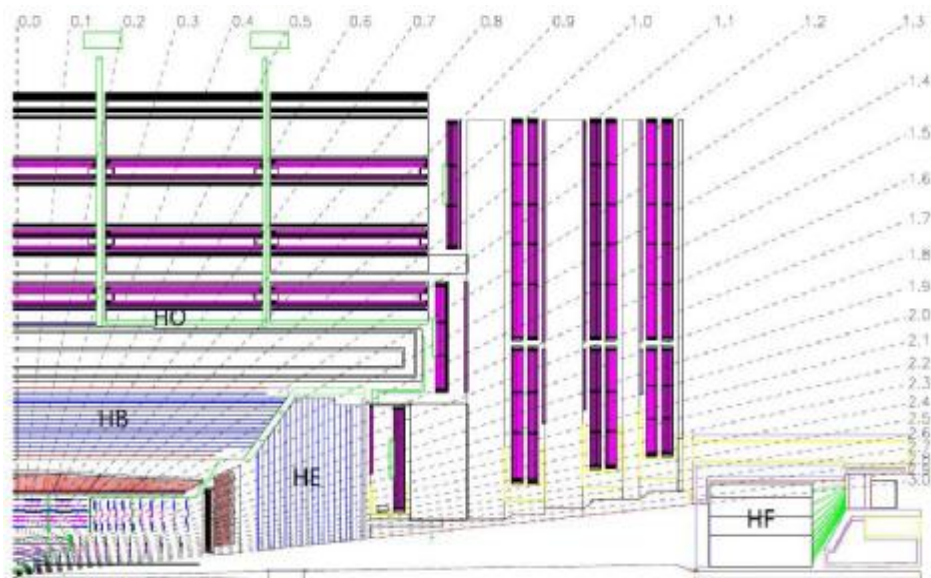
Figure 3.10. Longitudinal view of one quarter of the parts of CMS HCAL, HB, HE, HO and HF in the $r\eta$ – plane (CMS Collaboration, 2008)

The HB is placed inside the magnetic coil and covers the pseudorapidity range $|\eta| < 1.3$. The HB is divided into two sections, HB+ and HB-. Each section consists of 18 identical azimuthal wedges, resulting in a segmentation $\Delta\eta$ x Δf = 0.087 ´ 0.087.

The HE covers the pseudorapidity range $1.3 < |\eta| < 3$ and also divided into two sections, HE+ and HE- . They are placed in the end parts of the CMS detector with the ability of containing magnetic material. The granularity of HE is $\Delta\eta$ ´ Δf = 0.087 ´ 0.087 for $|\eta| < 1.6$, $\Delta\eta$ ´ Δf = 0.087 ´ 0.087 for $|\eta| \geq 1.6$.

HB and HE are sampling calorimeters, which consist of plastic scintillators as active material inserted between copper absorber plates, placed between the ECAL and the magnet.

The combination of HB and HE was not enough to absorb hadronic showers from particles with transverse energies greater than 500 GeV. To ensure these high energy shower containment in CMS, thus working as a tail catcher for $|\eta| < 1.4$, the

HCAL is extended outside the solenoid and is called HO. The amount of material till the last layer of HCAL can be seen in Figure 3.11 (ACHARYA, B. S. et all 2006).
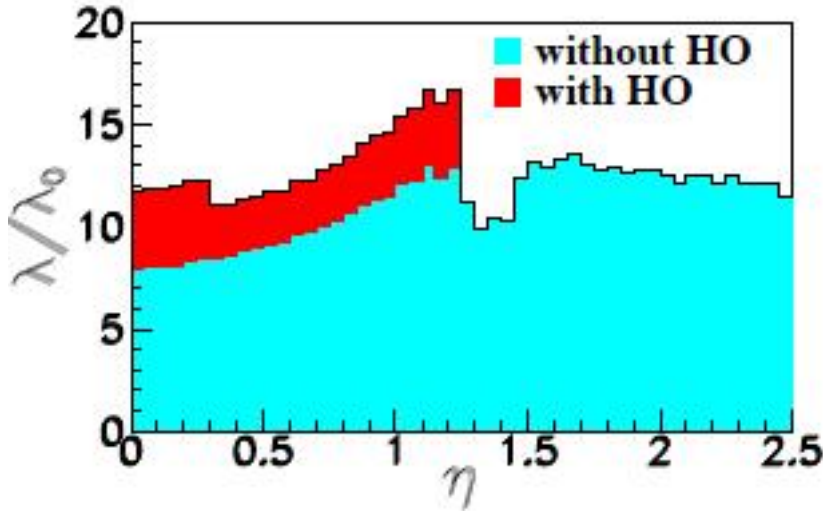
Figure 3.11. Number of interaction length as a function of η. The two shaded regions correspond to the setups with or without the HO (ACHARYA, B. S. et all 2006)

The HF is the last subdetector of HCAL and is designed to improve the measurement of the missing transverse energy and allows very forward jets to be identified and reconstructed. It covers the pseudorapidity range $3 < |\eta| < 5$.

3.2.5. The Magnet

One of the key elements of detector design is the configuration and parameters of the magnetic field. CMS has a solenoid magnet with a 4 Tesla magnetic field which is 100,000 times stronger than the Earth's magnetic field. A high magnetic field is required to make accurate momentum measurements of the TeV scale muons

The magnet is 13.5 m in length, 6.3 m in diameter and weighs 12000 tonnes. It has an inductance of 14 H. A view of the CMS magnet can be seen in Figure 3.12. The tracking system, the ECAL and the HCAL except HO is placed inside the magnet (Focardi, 2011).
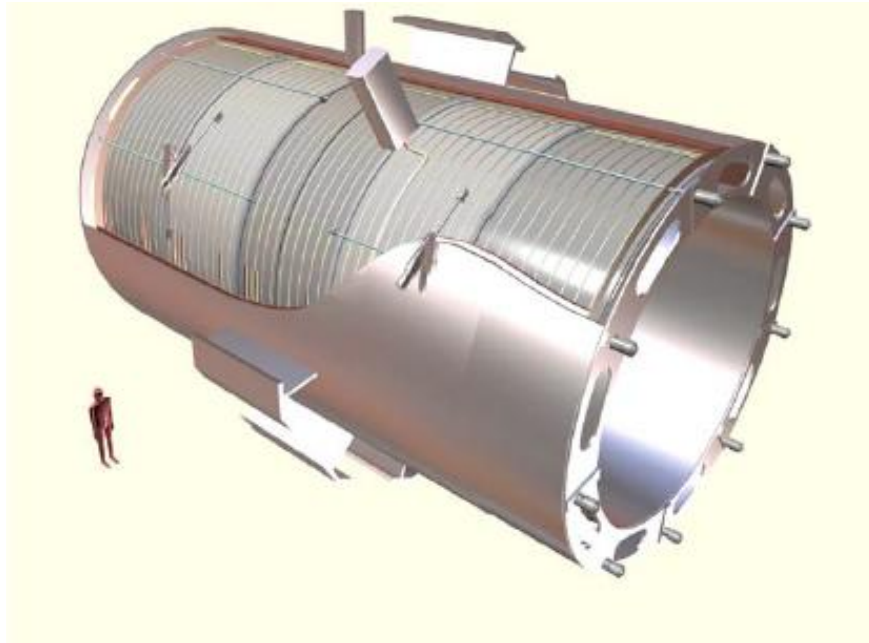
Figure 3.12. Artistic view of the CMS superconducting magnet
              (http://newsline.linearcollider.org/2011/05/05/one-hundred-years-of-
              superconductivity/cms-solenoid-magnet/)

The charged particles are identified from the curvature of the track that they follow in the magnetic field. The transverse momentum of a charged particle in a magnetic field, measured in GeV/c is given by

$$P_T = 0.3 \times B \times R \tag{3.1}$$

where B is the magnetic field in tesla and R is the radius of curvature of the charged particle in meters.

3.2.6. The Trigger and Data Acquisition System (DAQ)

There is no way to store all the data from proton-proton interactions at CMS which would be about one billion per second while CMS is performing at its peak. To produce a rare particle, such as Higgs boson, very large number of proton-proton interactions are required. On the other hand, not all of these collisions produce interesting events. Therefore a system that selects interesting events and reduces the

rate of events to be stored on computer disks is needed. Thus a trigger and a data acquisition system (DAQ) steps in. This is a two-step process: The Level 1 Trigger (L1 Trigger) and the High Level Trigger (HLT) (see Figure 3.13).

The L1 Trigger uses information from the muon chambers and calorimeters to select event signatures for interesting physics. It reduces the incoming average data rate to a maximum of 100 kHz, which was previously about a thousand kHz. The second step, HLT is a software system that uses the detector signals that pass the L1 trigger and reduces the rate of stored events by a factor of 1000.
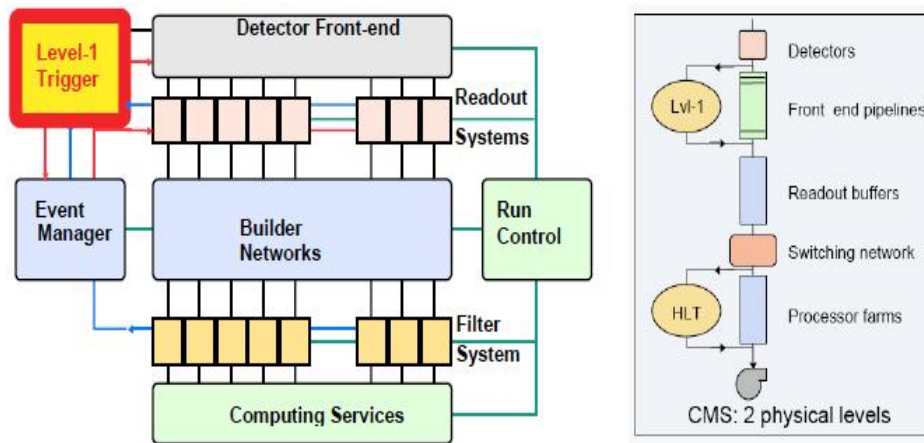
Figure 3.13. The CMS data acquisition system and Level 1 Trigger System
(http://arxiv.org/pdf/0810.4133.pdf)

4. INSTALLATION AND COMMISSIONING WORK IN HCAL

4.1. Light Emitting Diode (LED) Stability of the HB and HE Detectors

LED information is used for the calibration of a detector, to determine the lost or unstable channels, to monitor the gain stability and to identify the timing shifts. The detector channels are tested by sending light to the detector, while there is no beam.

This analysis was done to check the calibrations of the sub detectors HB and HE using local LED runs. LED signals with some specific voltages were sent into the calorimeters, and the uniformity of the responses from the hybrid photo diodes (HPDs) in different parts of the calorimeter is studied.

There are 1296 channels of both HB+ and HB- , therefore HB contains 2592 channels in total. Similarly HE has 2592 channels, 1296 for HE+ and 1296 for HE- . Each LED data set includes 2000 events, hence the energy of a channel of each data set is an average value over these 2000 events. In this analysis the mean and root mean square (RMS) values of this energy are calculated and how various channels of calorimeters change with respect to each other is investigated for each specific data set. What is done for one data set was repeated for all LED data sets. In this way, if there is a problem it was possible to decide whether the problem belongs to the channel or to the data set. 295 local data sets, which were taken between May 2010 to December 2010 (run number 134783 to 151621) were used in the analysis.

The histograms of average LED energy were first studied individually for HB+ and HB- and similarly for HE+ and HE- to understand which sub detector is responsible for a problem that might occur. The plots are pretty much stable (Figure 4.1 shows the HB+ and HB- histograms). When the average energy of the sub detector HB+ is divided by the average energy of HB–, the average energies of these two detectors seem to be compatible with each other (Figure 4.2).
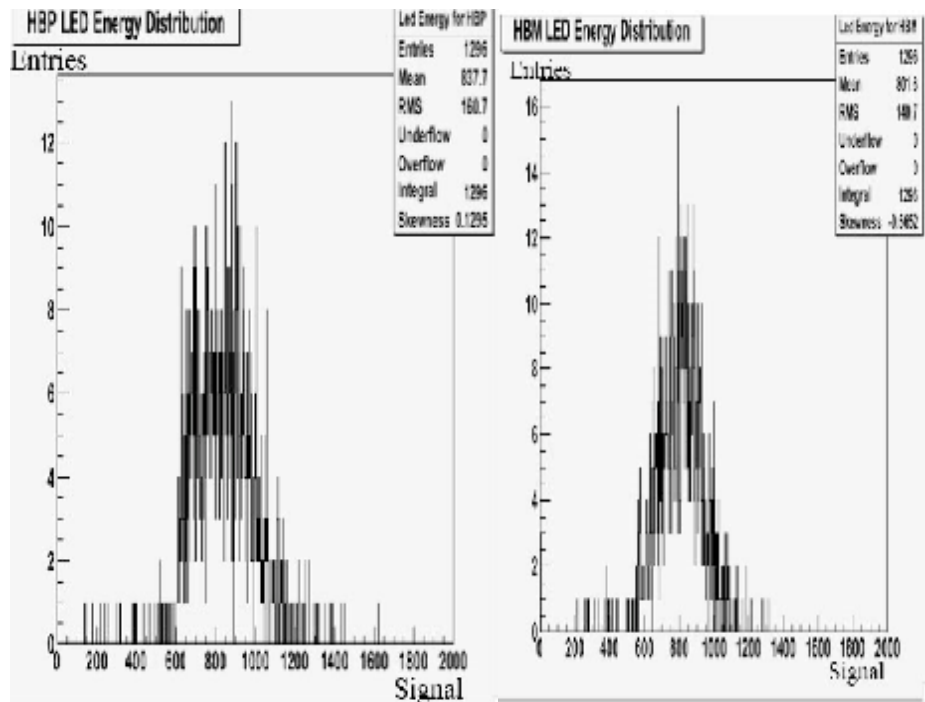
Figure 4.1. Histograms of average LED Energy for HB+ (left) and HB− (right)
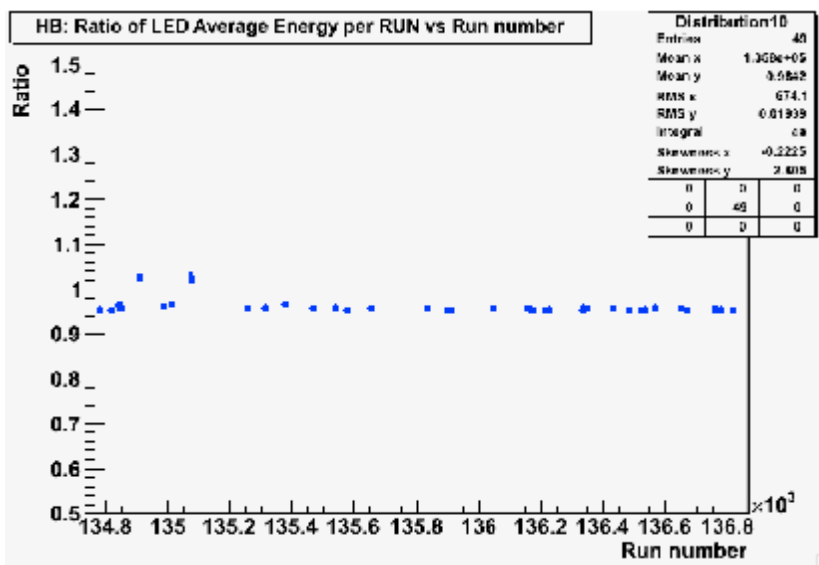
Figure 4.2. Ratio of the LED average energy of HB+ to HB-

After calculating the ratio of the average LED energy, the histograms of average LED energy for both HB and HE are plotted (Figure 4.3 shows the HE histogram). While plotting the histograms, LED signals were used as known input to different channels and output signals of each channel were checked. Energy signal is

in ADC counts. There was no data for HE in channel eta: -19, phi: 43, depth:2. This is why we have 2591 entries instead of 2592. This was a known problem.
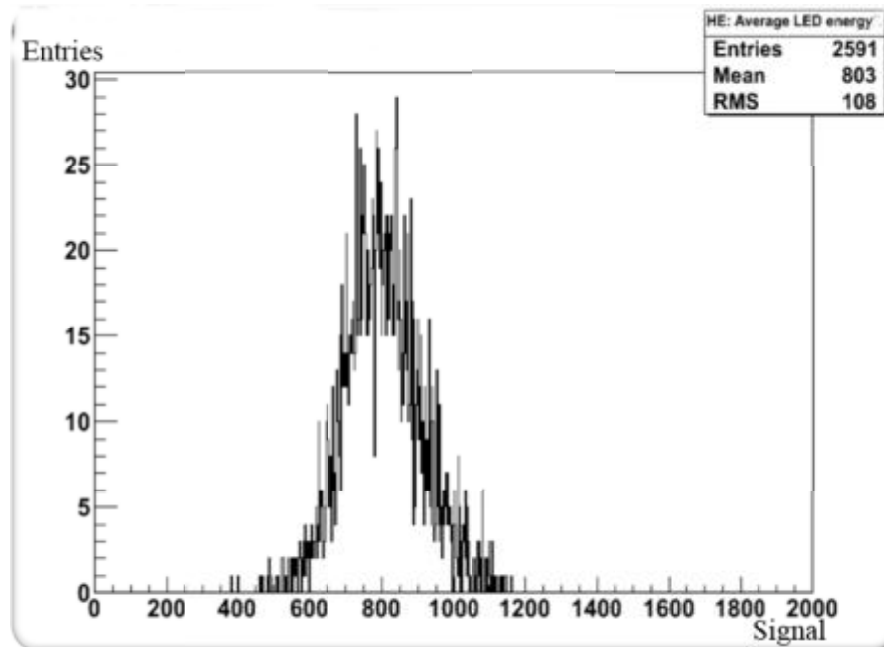
Figure 4.3 Histogram of the average signal for channels of HE over all runs

For the next step LED RMS energy is divided by the mean energy over runs and a cut is put at 0.05 value of this ratio and the channels having a value greater than this cut are determined (Figure 4.4. and Table A.1). The reason of using relative RMS signal is to eliminate the calibration differences between channels.
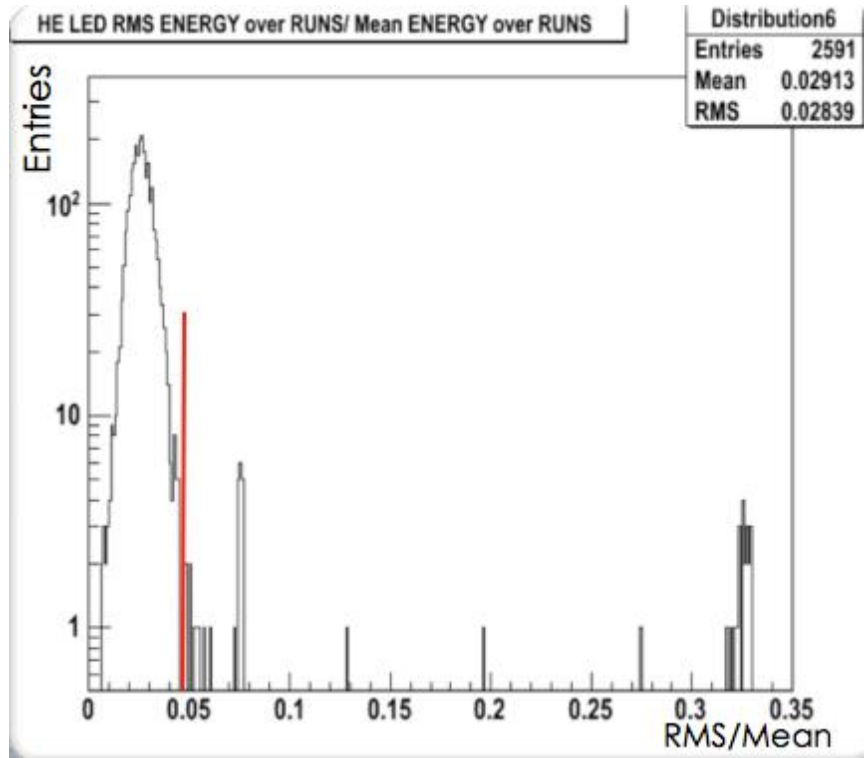
Figure 4.4. Histogram of the HE LED RMS energy over runs divided by mean energy over runs

4.1.1. Normalization Method

In order to eliminate the common shifts in HB and HE which were seen in specific channels, a three-step normalization method was used.

1) The signals were summed over all channels and divided by the number of channels. The value obtained was called 'average signal'. The plot of average signal values versus run number for HE is shown in Figure 4.5.

2) The energy values from the sub-detectors are divided by this average value.

3) The signal values obtained after this normalization were used in place of the original signal values in the graphs (Figure 4.6).
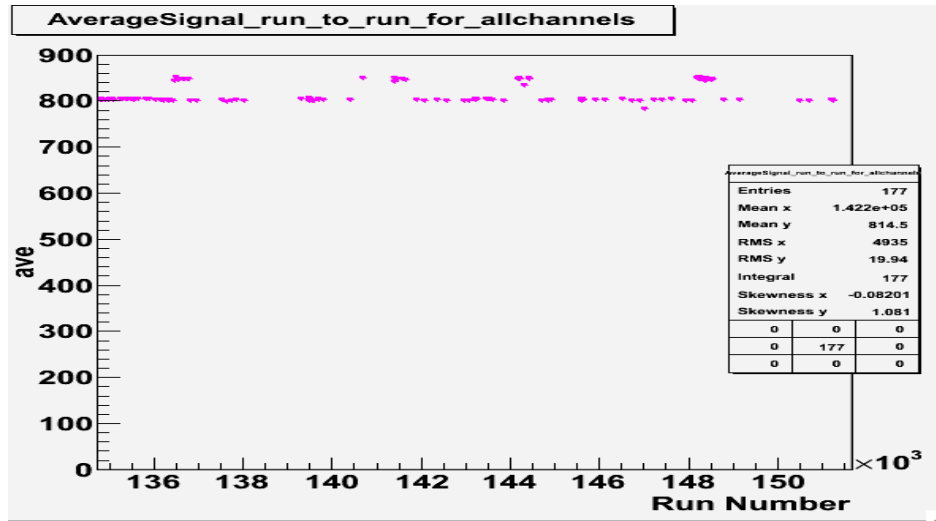
Figure 4.5. Average signal values versus run numbers after normalization
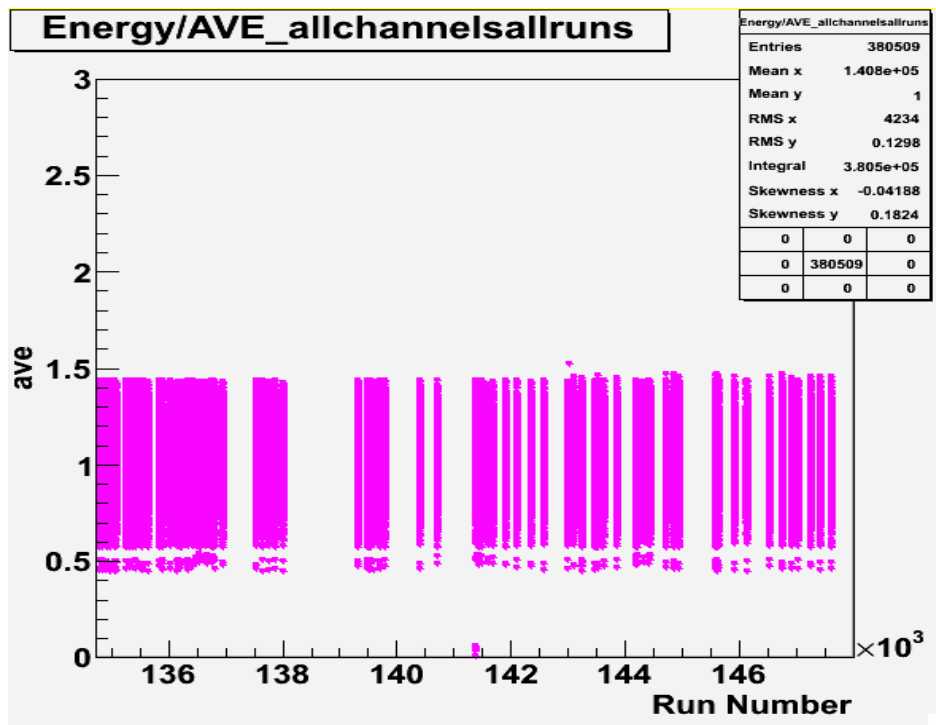
Figure 4.6. Obtaining the normalized signal for each run. Energy values divided by the average energy versus run numbers

Last but not least the histogram of the relative RMS values for each channel over all runs is plotted (Figure 4.7) and channels which still have a value greater than 0.05 are determined and given in Table A.2.
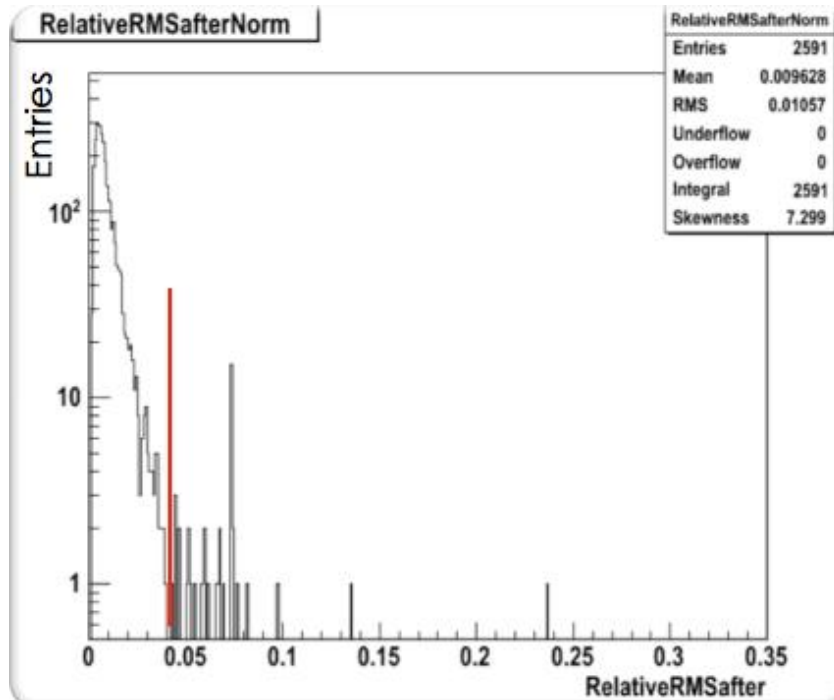
Figure 4.7. Histogram of the relative RMS values for HE after normalization

The plot of the ratio of the RMS values to mean values i.e. relative RMS before and after normalization for the channel with one of the worst results (21, 45, 2) can be seen in Figure 4.8(a).
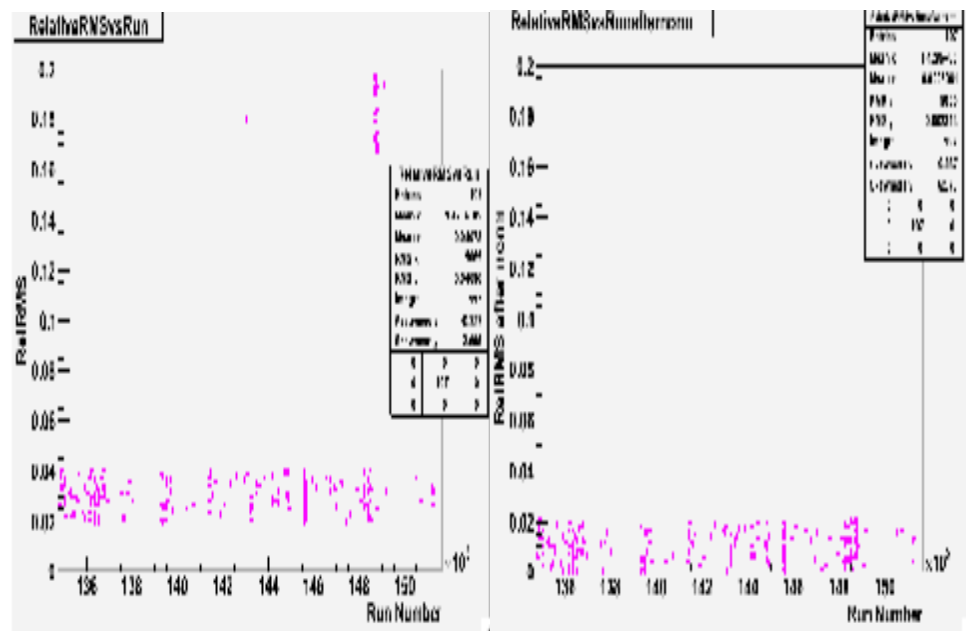
Figure 4.8.(a) Relative RMS values before (left) and after (right) normalization for channel (-21,45,2)

In order to understand how normalization works on a channel with good relative RMS values, relative RMS versus run number for channel (26,33,1) which already has a low relative RMS value was plotted (See Figure 4.8 b).
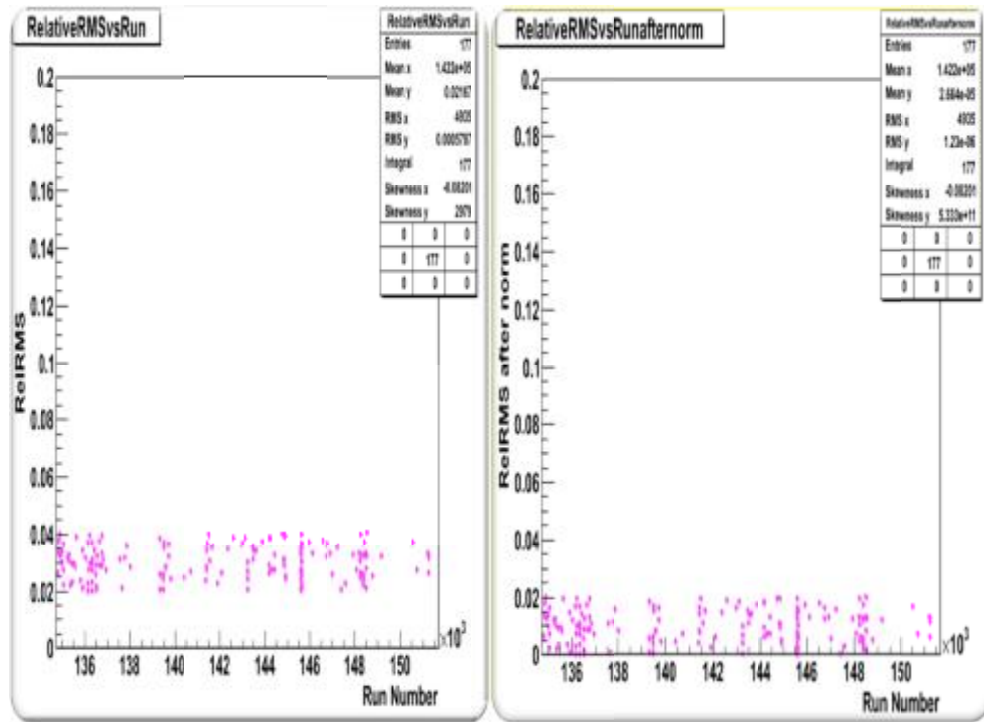
Figure 4.8.(b) Relative RMS values before (left) and after (right) normalization for channel (26,33,1)

As can be seen from Figure 4.8 (b) a good channel's relative RMS value moves down only a little bit with normalization.

To summarize this analysis; relative RMS values for each channel are checked to eliminate the calibration differences between channels. Some channels seem to have higher relative RMS values than expected and a normalization method explained in the text is used to get rid of them. After normalization, an improvement is seen in relative RMS values of channels.

4.1.2. Fractional Signal Change Method

In order to investigate if the observed energy values change from run to run a ratio was obtained by dividing the difference of the signal of a run and the signal of the previous run by the signal of the first run.

$$\text{Fractional Signal Change} = \frac{\text{Signal of a run} - \text{Signal of the previous run}}{\text{Signal of the first run}} \qquad (4.1)$$

These ratios were plotted against the run numbers for both HB and HE. An example can be seen for HB in Figure 4.9.
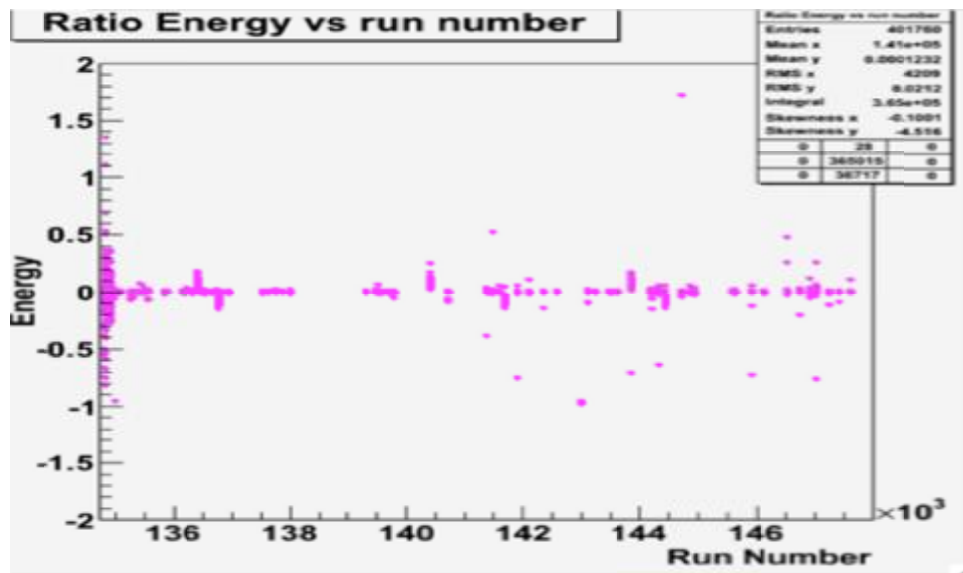
Figure 4.9. Fractional signal change versus run number and histogram of the fractional signal change for HB

From these plots, runs with bad fractional signal change values were identified and these values for these specific runs were plotted in 3D as a function of eta and phi to see the problem in detail. An example of these plots can be seen in Figure 4.10. These plots show that the problem is not limited to certain eta or phi values, but is spread over the whole range.
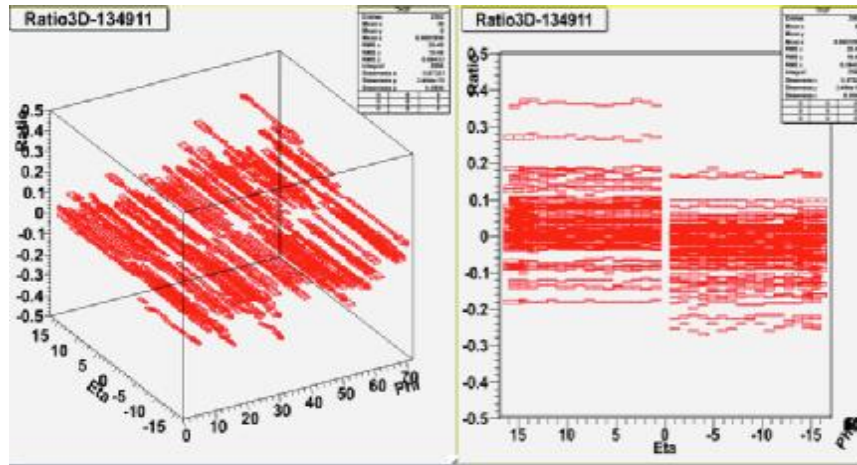
Figure 4.10. Plot of 3D fractional signal change for run number 134911

4.1.3. Results

By using normalization method the shifts in specific channels of HB and HE sub detectors were eliminated. RMS/Mean LED signal values were over than expected for HE (- 21,45,2), HE (- 20,45,1) and HB (- 13,7,1). Run numbers 135078, 135651,135908,136046,136175,136175,136175,143022,148701,148708,148709, 148711,148715,148716,148717,148720,148722,148732,148746,148759,148766, 148767,148768,148769,148770,148771,149086 are found to be bad runs with bad fractional signal change values even after the normalization procedure and extracted from the future analyses.

4.2. HB HE ENERGY RECONSTRUCTION

The energy containment of the pulse shapes of sub detectors HB and HE are investigated in this analysis to find methods to reduce the effects of pile up. 1000 events are reconstructed using 4 time slices and 2 time slices (In the LHC each 25 nanosecond of time unit is called one time slice). The data sample used in this analysis is the HT primary data set (/HT/Run2011A-v1/RAW) for run 161311. This run was the last run in 75 ns beam spacing. The effects of out of time pile up is smaller than 50 nanosecond beam spacing.

Generally, HB/HE signal pulse starts in time slice 4. The containment of signal is roughly 70% for ts4, (20%) for ts5 and (8%) for ts6. Two time slices should contain roughly 90% of signal. Therefore in this analysis 2TS RECO which has 90% of the signal and 1TS RECO which has 70% of the signal are studied. The RECO (a CMSSW data format containing the relevant output of reconstruction) which was in use before this analysis used 4TS. Two sets of HBHE rechit (reconstructed hit) collections are kept in each event in order to make comparison of energy scale with 4TS and 2TS, i.e. $E(2TS)/E(4TS)$, where ;

$$E(2TS)=E(ts4)+E(ts5) \tag{4.2}$$
$$E(4TS)=E(ts4)+E(ts5)+E(ts6)+E(ts7) \tag{4.3}$$

The HCAL reconstruction, apply a correction to the containment, depending on the number of time slices and energy. The energy dependent correction is needed because of "time slew"- smaller signal comes out QIE several seconds late. An example of the HCAL pulse shape can be seen in Figure 4.11. This is the analog signal coming from HPDs which convert the scintillation light from the scintillator tiles in the gaps in HB or HE, produced by particles hitting HB or HE, into analog electric signals. It is peaking at about 15 ns and then starts falling.
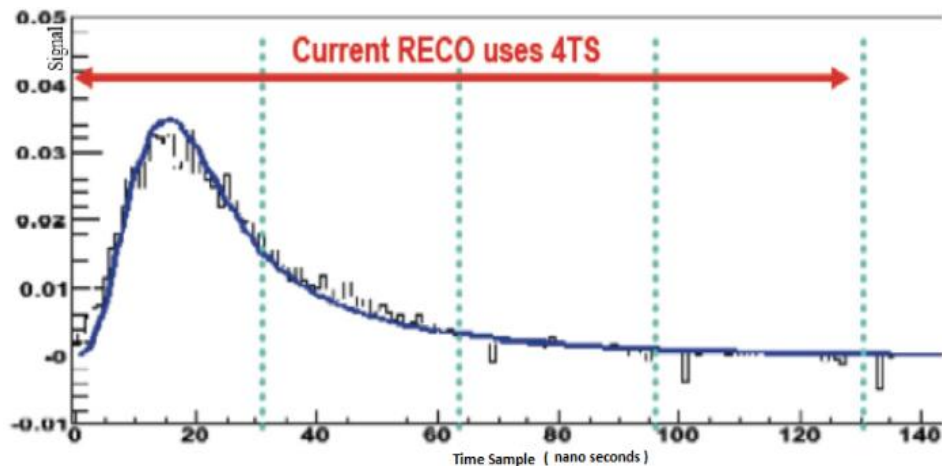
Figure 4.11. HCAL Pulse shape. From left to right TS4, TS5, TS6 and TS7 and TS8

The analog signal goes to QIE (charge integrating electronics) to produce the digital signal (ADC counts). An example of such a digitized signal is shown in Figure 4.12. The *x*-axis is time slice (TS) number. The first 25 ns in Figure 4.11 corresponds to TS = 4 in Figure 4.12, the second 25 ns to TS = 5 and so on.

Firstly, to understand in which time slice (TS) bins the energies of the signals produced in HB and HE sub-detectors were collected, the energy contents of the signals in different energy intervals were investigated and plotted into histograms. (see Figure 4.12).
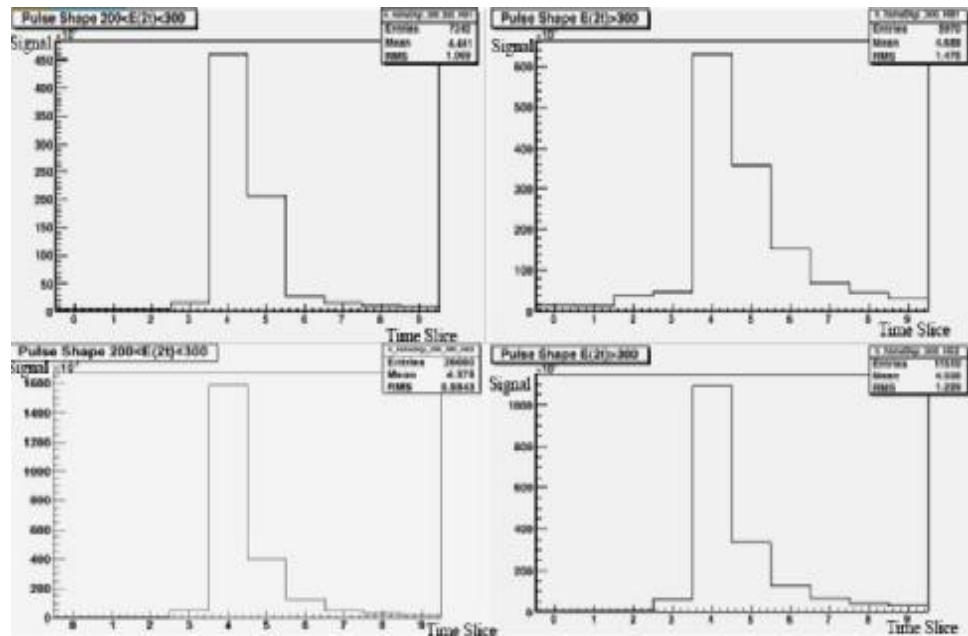
Figure 4.12. Pulse shapes for HB + (top) and HE – (bottom) for different energy intervals: $200 < E(2\text{ts}) < 300$ (left) and $E(2\text{ts}) > 300$ (right)

There is an unexpected signal in time slice 2 for HB which was a known problem caused by HPD/RBX noise.

Later, we changed the present phase setting to 4.0 ns which was (- 3 ns) before and lowered the energy scale by 1.03 for 2 TS RECO but not for 4 TS RECO. Pulse shapes for different energy ranges are examined with the new and old phase settings for 2TS (see Figures 4.13 (a) and (b))
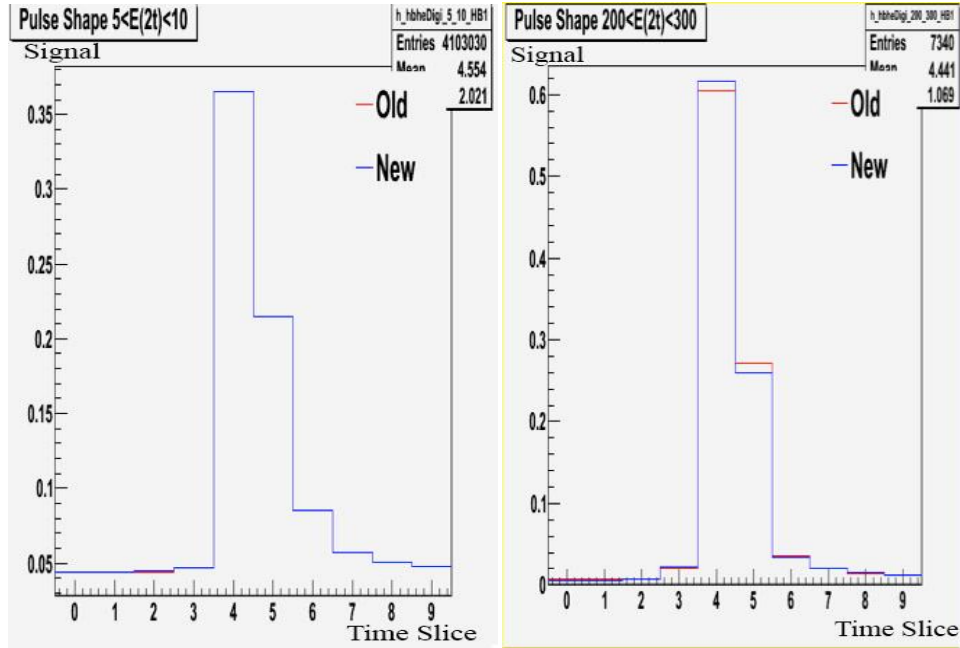
Figure 4.13.(a) Energy signals vs time slice in 2TS for energy interval $5 < E(2TS) < 10$ for HB+   (b) Energy signals vs time slice in 2 TS for energy interval $200 < E(2TS) < 300$ for HB+

There is almost no effect for low energies but some small differences could be seen in higher energies for time slice 4 and 5.

For the second step, different energy ranges for $E(2TS)/E(4TS)$ and $E(1TS)/E(4TS)$ are compared with each other to understand how much do the energy values for the reconstructed events change (see Figure 4.14 and 4.15).
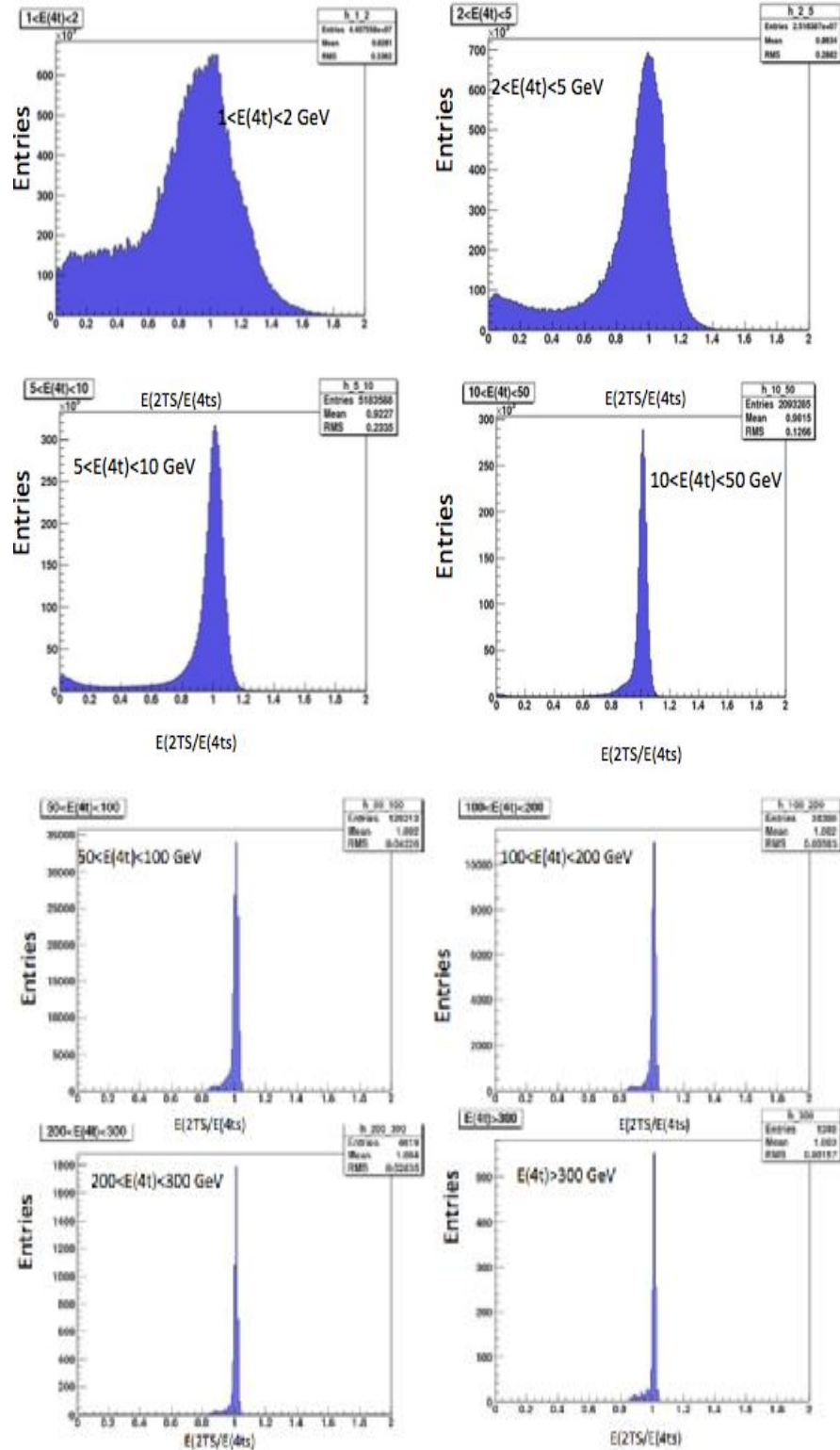
Figure 4.14. $E(2TS)/E(4TS)$ values for different energy ranges
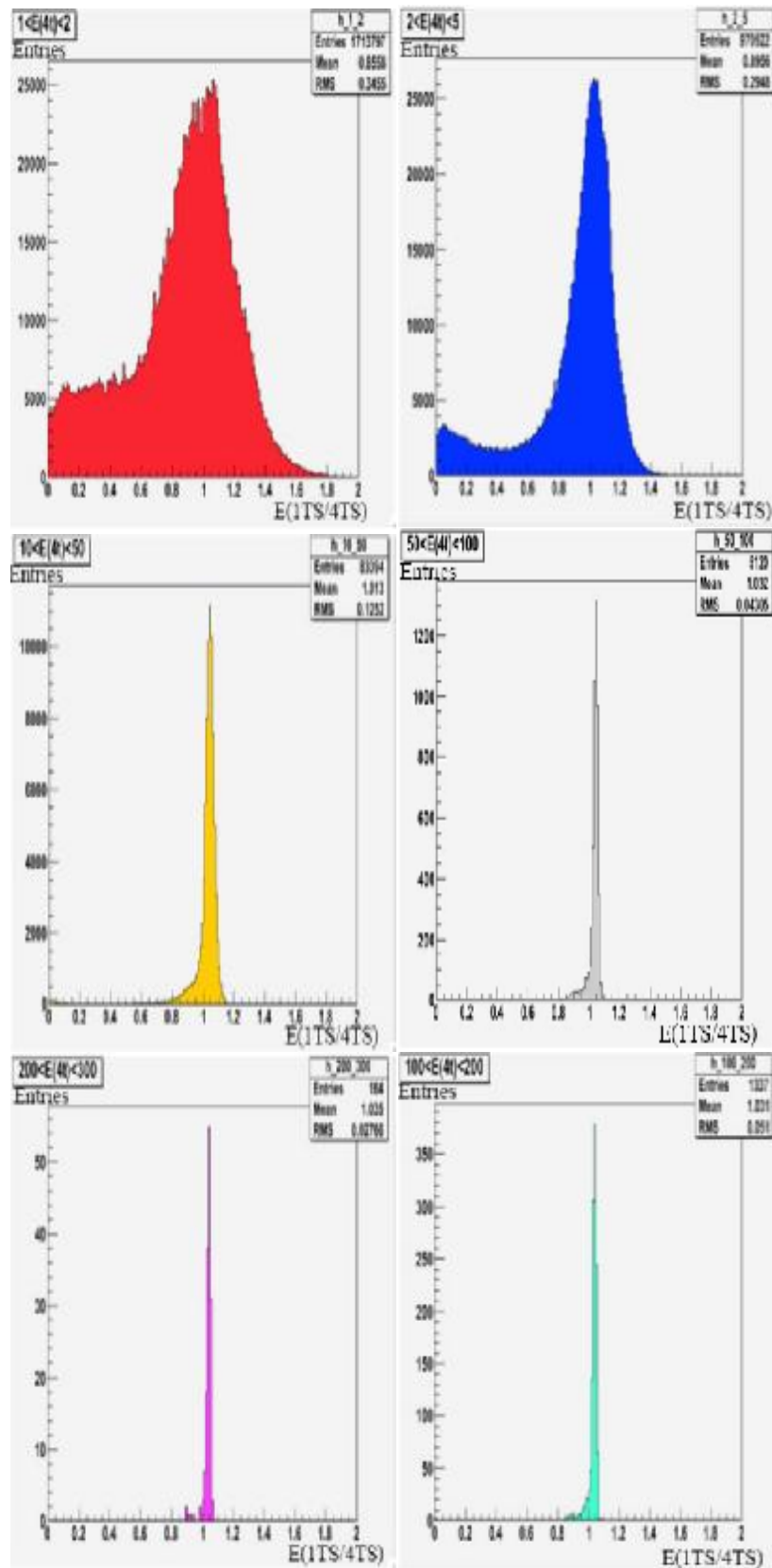
Figure 4.15. E(1TS)/E(4TS) values for different energy ranges

In higher energy intervals the reconstructed energy values for both 2TS and 1TS are better than lower energy intervals. As a last step the mean values of energy are checked for 1TS and 2TS using different phase settings which were 10 ns, 7ns, 1ns, - 2ns and 4 ns (See Figure 4.16). A positive phase setting means a shift to the right and a negative one means a shift to the left.
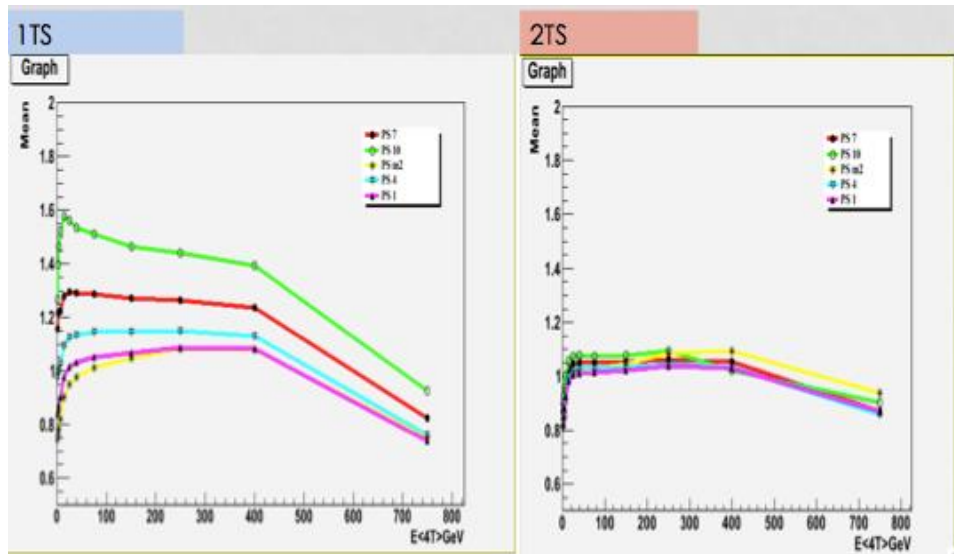
Figure 4.16. Mean values for 1TS (left) and 2TS (right) using different phase settings for run number 161311

Different phase settings didn't make a dramatic change for the mean energy value for 2TS while it did for 1TS. Finally phase setting was agreed to be chosen as +4 ns.

4.2.1. Results

As can be seen from Figures 4.17a and b, the distribution of the mean energy of HCAL stabilizes for 2TS RECO samples for the phase setting +4 ns.

The conclusion of this study is that, in order to minimize the effects of pile up 2TS RECO samples should be used instead of 4TS RECO samples and phase setting should be taken as +4 ns.
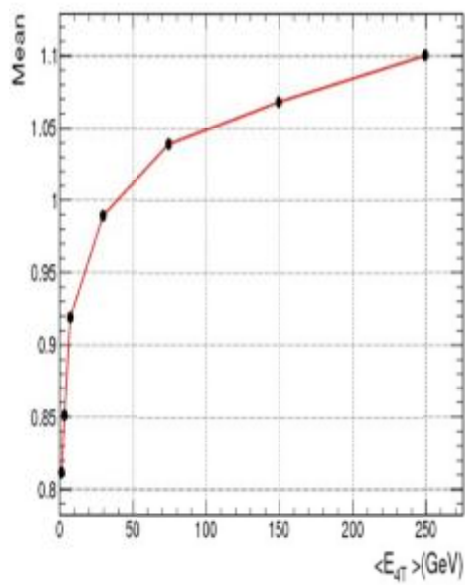
Figure 4.17(a) Mean Value of the Energy for 2TS RECO with phase Setting - 3
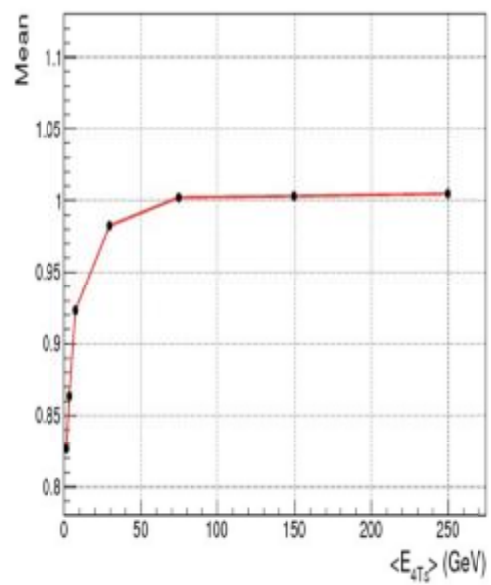
(b) Mean Value of the Energy for 2 TS RECO with phase setting +4

5. MUSCLE FIT ANALYSIS

Good muon measurement is crucial for many physics analyses in the CMS experiment. The momentum measurement of muon tracks is affected by many factors like systematic uncertainties due to the insufficient knowledge and incorrect mapping of the detector material, mismodeling of the magnetic field and problems of the reconstruction algorithms used to fit the track trajectory. It is also very sensitive to the precise alignment of the silicon sensors of the tracker which is the innermost subdetector and of the muon chambers which are the outermost subdetectors of the CMS detector. Measuring the momentum scale and resolution is important to understand the effects mentioned above and can be achieved using the two-body decays of neutral particles from proton-proton collisions. The momenta of such muon pairs change between a few GeV and a few hundred GeV and therefore are not very useful for a direct check of the momentum measurement of TeV energy tracks but they provide a very valuable tool to spot deficiencies in the Monte Carlo (MC) description of the detector and this is beneficial to tracks of any momentum. A well-calibrated momentum scale is a must for the precision measurements of the top quark and W boson masses, for B-hadron spectroscopy and for some other first-class measurements expected from the CMS detector.

The production cross-section of di-muon decaying neutral resonances is large at the LHC, therefore large samples can be obtained even with a few inverse picobarns of luminosity as can be seen in Table 5.1 (Bolognesi, Borgia, Castello, Mariotti, De Mattia, Dorigo, 2010). Note: cross sections are derived from Pythia and should be understood as order-of-magnitude estimates. In particular, the quoted J/ψ and $\Upsilon(2S)$ yields do not account for production through decays of B hadrons or excited charmonium states; likewise, Υ yields do not account for decays of excited bottomonium states.

Table 5.1. Cross sections, branching fractions to muon pairs (Bolognesi, Borgia, Castello, Mariotti, De Mattia, Dorigo, 2010), and di-muon yields per 10 pb[-1] in 10 TeV proton-proton collisions for the di-muon resonances used in this study

Particle	s_{pp}(nb)	B (m^+m^-)	Produced events / 10 (pb[-1])
Z	67.6	0.03366 ±0.00007	22,740
J/y	2145.0	0.0593 ± 0.0006	1,272,000
Y(2S)	289.2	0.0075 ± 0.0008	21,690
Υ(1S)	560.5	0.0248 ± 0.0005	139,000
Υ(2S)	328.0	0.0193 ± 0.0017	63,300
Υ(3S)	81.7	0.0218 ± 0.0021	17,800

In this analysis, the track momentum measurement is corrected and its resolution is precisely determined using the muon pairs from J/y s collected during the 2011 data taking period. The reason for choosing J/y decays is obvious from Table 5.1; it is the resonance with maximum production cross section and highest branching ratio for decays into muon pairs.

5.1. Introduction

The measurement of charged track momentum is affected by the reconstruction capability and our limited knowledge about the physical configuration of the detector. The main sources of biases in the momentum measurement are from residual misalignments and weak-modes, imprecisions in the magnetic field model, mismodeling of the material distribution and density. These effects lead to some biases which are hard to eliminate. In this analysis an algorithm called MuScleFit (Bolognesi, Borgia, Castello, Mariotti, De Mattia, Dorigo, 2010) is used to correct for these effects and extract an estimate of the transverse momentum resolution. To calibrate the data with a reference model of the J/y, an unbinned likelihood fit is used.

In this study, first, the data and the simulation will be compared to find possible biases in the momentum scale. Then, suitable functions will be developed to correct these biases and finally the results of the correction and the resolution fit will

be presented. In the last section a comparison with the results using the 2010 data will be given.

5.2. The MuScleFit Algorithm

5.2.1. An Outlook On MuScleFit

An algorithm, that is capable of extracting the needed information from the combination of the reconstructed kinematics of the muon pair, with the knowledge of the parent particle species is developed to solve the problems mentioned in the introduction part in section 5.1 and is called The MuScleFit (Muon Scale Fit) Algorithm (Bolognesi, Borgia, Castello, Mariotti, De Mattia, Dorigo, 2010).

The close connection between the momentum scale and resolution in the determination of potential biases on measurements can be seen easily: a possible bias in the momentum scale can be meaningfully deduced from the measured di-muon mass on an event-by-event basis only if a value is assumed for the uncertainty in the four-momentum of the daughter tracks, from which mass resolution can be estimated. The finite mass resolution hides the scale information but one can fully recover it by a multi-parameter likelihood fit. Once one defines a set of functions describing the dependence of the biases − offsets from the true values - on track kinematics and of the measurement resolutions, the best estimate of the parameters of those functions can be determined by minimizing a likelihood, provided that a sufficient set of homogeneous data is used.

Describing the biases and resolutions with precision is a key element for this study. Oversights of the detector material, alignment of the devices, magnetic fields, tracking reconstruction are related directly with the features of biases and resolutions.

5.2.2. The structure of the algorithm and its technical implementation

MuScleFit algorithm is accomplished in the form of an analysis module that is capable of running serially multiple times on the same input file (Bolognesi, Borgia, Castello, Mariotti, De Mattia, Dorigo, 2010). Such architecture meets the requirements for the need of an iterative processing of the data, which allows the user to get the parameters of correction function in one iteration, and in a second pass verify that the application of those corrections on the same data produces an unbiased output; an iterative correction can also be thought of in particular cases, when convergence to the best result can only be obtained after a few cycles.

A first iteration is performed while the momentum scale of tracks is kept fixed, to allow the algorithm to seek only a working estimate of the parameters modeling the shape of the mass distribution of background events. After the determination of those parameters with some accuracy, a second iteration minimizes the relative function, to look for a modification of the momentum scale while keeping the formerly determined background parameters fixed. Completely customizable multiple steps with equally simple configurations can be done.

5.3. Data Sets

This analysis was performed with the 221 pb^{-1} of 2011 data collected by theDoubleMu3_Jpsi_v1 and DoubleMu3_Jpsi_v2 triggers (double muons coming from J/ψ s). To allow comparison with MC a consistent simulation was used. This analysis is performed using CMSSW_4_2_4.

The root trees that were used in the analysis are: TTree Onia2MuMu V9 PsiToMuMu Summer11 PU.root as MC and TTree Onia2MuMu V9 May10ReReco v1.root as data.

5.4. Muon Momentum Scale Biases in Data and Simulation

The first step of this analysis is to find the possible biases in the momentum scale. A peak is fitted by a Crystal Ball (CB) fit (Appendix B) on the di-muon mass distribution in the J/ψ range as a function of a set of kinematic variables of the single muons. Deviations from the expected distribution points out a bias.

Figure 5.1 and Figure 5.2 show the mass distribution of positive and negative muons as a function of the η for Data and MC respectively. Note that the CB fit peak is dependent on the resolution. The resolution is better and the peak is higher in the barrel. The resolution is worse and the peak is expected to return a lower mass in the endcaps. However, there is a charge dependent bias: the distribution is higher than expected in the positive η region for negative muons and negative η region for positive muons. By looking at the p_T distribution (Figure 5.2) one can see that there is a bias in low p_T (up to 5 GeV).
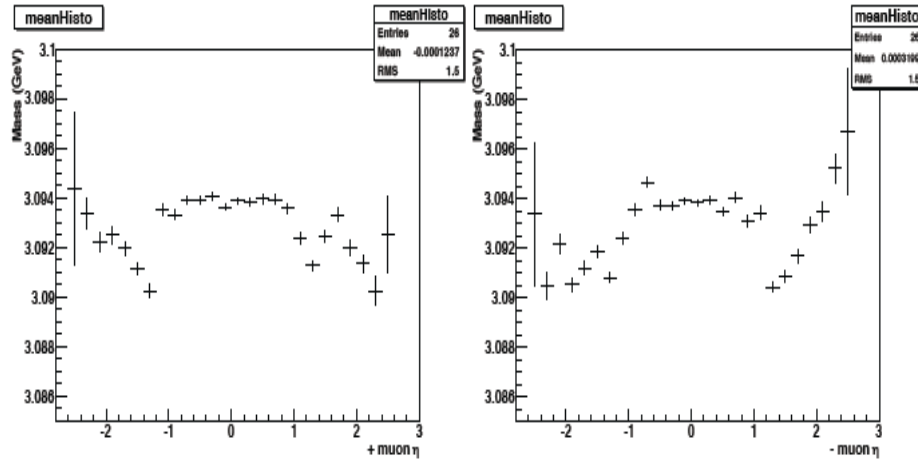
Figure 5.1. CB peak versus muon eta for positive (left) and negative (right) charged muons for Data
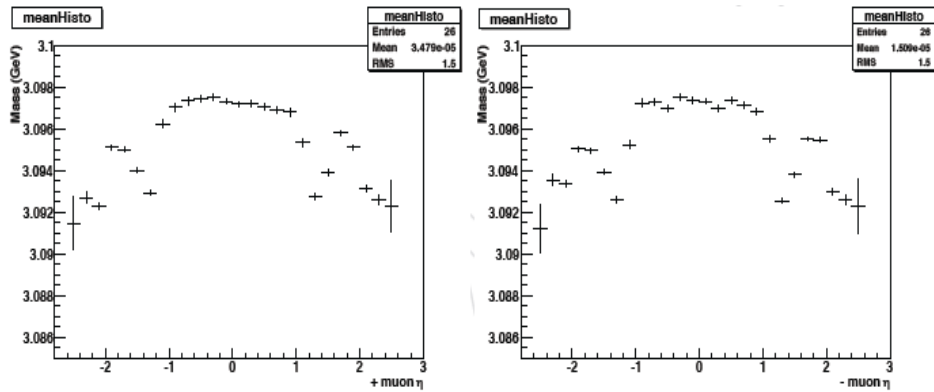
Figure 5.2. CB peak versus muon eta for positive (left) and negative (right) charged muons for MC
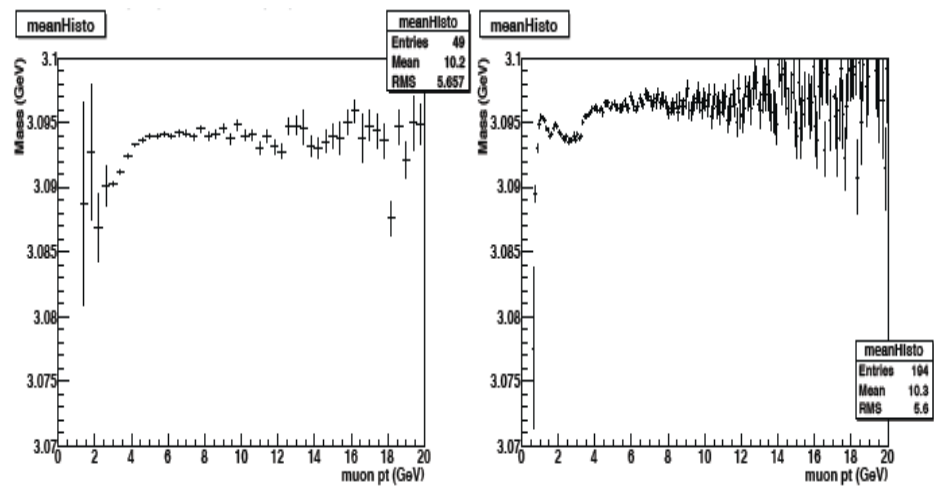
Figure 5.3. CB peak vs muon p_T for Data (left) and MC (right)

In the next step ansatz functions will be used to make corrections in the momentum scale and mass resolution.

5.5. Ansatz Functions

The term "ansatz" refers to any attempt to write down a trial solution in parametrized form. This term is derived from the German word "Ansatz" which literally means "approach"; that is, an ansatz is a certain way of approaching the problem by an educated guess of a particular functional form. It is verified later by its results.

5.5.1. Scale Correction

Considering the shape of the biases in data and after trying several functions (of the order of 30 in number) the following ansatz function with 8 parameters is chosen:

$$p\phi_T = par[1] \cdot p_T \cdot (1+f(\eta)+g(p_T)) \tag{5.1}$$

where

$$f(\eta) = par[2] + par[3] \cdot \| \eta | - par[5]\| + par[4] \cdot (|\eta| - par[5])^2 \tag{5.2}$$

$$g(p_T) = par[6] \cdot (p_T - par[8]) + par[7] \cdot (p_T - par[8])^2 \text{ for } p_T < par[8] \tag{5.3}$$

Same ansatz function is used to calibrate the MC simulation. This ansatz function has a parabolic correction at high positive pseudorapidity for negative muons and at high negative pseudorapidity for positive muons. This is done to correct the related biases in these regions which can be seen from Figure 5.1. Also a parabolic correction is performed to get rid of the scale in low p_T regions that can be seen from Figure 5.3.

5.5.2. Resolution

A binned function with 12 bins symmetrical with respect to the y axis is used in this study. Allowing flexibility and making each bin independent by removing the correlations between the parameters are reasons to use a binned function. Resolution function has 12 bins in η for $\sigma(p_T)$, one value for $\sigma(\mathsf{f})$ and one for $\sigma(\cot(\theta))$ for a total of 14 parameters.

5.5.3. Background

5.5.3.1. Selection of the Background Fit Function

The background distribution must be modeled as the last essential ingredient to perform the calibration on data. Since the background is almost flat and does not depend on the resolution strongly, it is determined externally from the main likelihood fit. The background is fitted with a CB plus exponential pdf in bins of the η of the two muons after the trigger selection. The background fit is improved by adjusting the binning at high pseudorapidity. The bins used for each muon are 0.85, 1.25, 1.6, 1.8, 2.0, 2.2 and all possible combinations are used thus building a 2D map. Figure 5.4 shows an example of the fits for one of the bins in the barrel and one in the endcaps. Background doesn't change much for different regions.
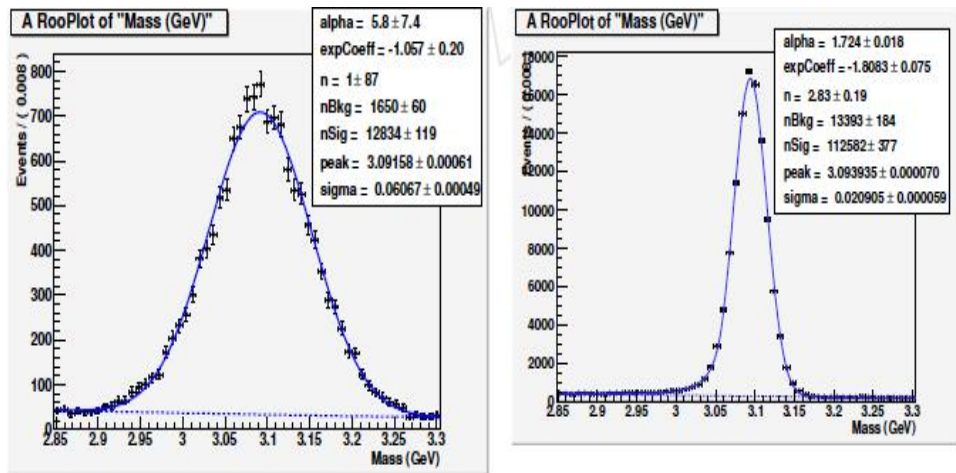
Figure 5.4. Background model for endcap (where η of the first muon is between 2.0-2.2 and second muon is in the regions $|\eta| > 2.2$) and barrel (Where both muons are in $|\eta|<0.85$)

In the next step, background is taken only from the side bands, i.e. the peak is dismissed and an exponential fit is used for the side bands. The reason for doing this is to see if the backgrounds with and without the signal are consistent with each other. An inconsistency indicates that some part of the signal might be background. It was observed that the exponential fit applied to the side bands only was not

successful and it was decided to use a CB plus exponential fit to the data (Figure 5.5).
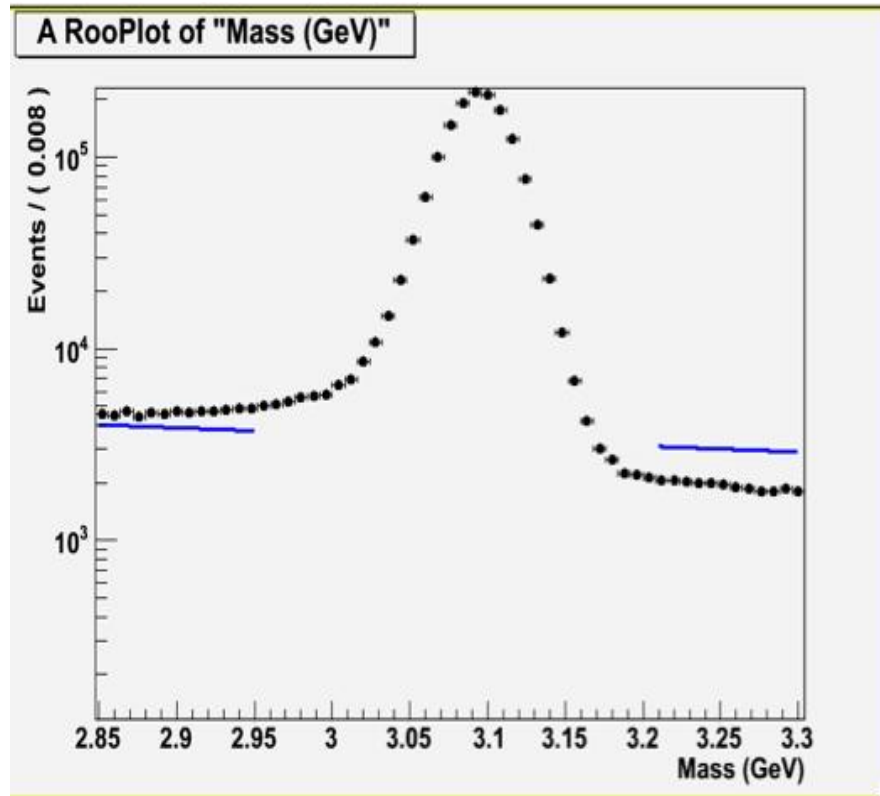
Figure 5.5. J/ψ mass plot with side bands only background fit

5.5.4. Selection of the MC

In order to choose the simulation data to be used in this analysis, the data from newTree_Summer10JPsiPromptSTARTUP.root (old MonteCarlo) and TTree_Onia2MuMu_V9_JPsiToMuMu_Summer11_PU.root (new MonteCarlo) which was produced during summer 2011 were compared.

In this step MuScle Fit algorithm is used to get the resolution and scale fit results and the results from old and new MonteCarlos are compared with each other. An unbinned likelihood fit with a reference model is used to correct the momentum scale. To understand the sources of all possible biases mass resolution is plotted.

Using the MuScleFit program, the shift of the mass values of the muon pairs coming from J/ψ decays with respect to the measurements were corrected with the help of proper ansatz functions. The resulting mass versus momentum plots are given in Figure 5.6. The plots in Figure 5.6 (and also Figure 5.7) are the result of CB fits on slices of a two dimensional histogram with mass along y axis and muon p_T along x axis. The number of entries in this histogram is equal to the number of J/ψ candidates. In the plots of Figure 5.6 (and also Figure 5.7) the mass value for each p_T bin is given along the y axis. In order to extract this value, a CB fit is done for each p_T bin and the value of the mean of the CB function is taken as the mass belonging to that bin. These plots will always have the same entries equal to the number of p_T bins; the cuts which will be used may change the number of entries in the original histogram but will not effect the number of the entries in these plots.

These plots were filled twice for each event, once for each muon of the muon pairs. The data points before the calibration are shown black and the data points after the calibration are shown red.
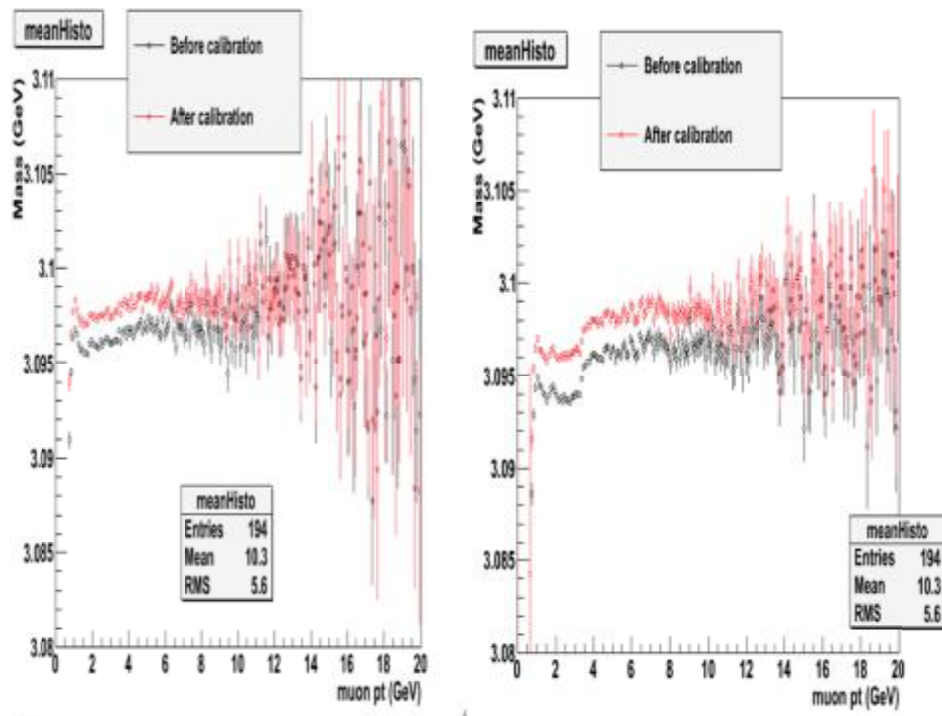
Figure 5.6. Mass versus momentum plots of muon pairs for the old (left) and new (right) MCs

As can be seen in the Figure 5.6 there is a sudden drop around 3 GeV for the new MC. To check if this drop was due to J/ψ s which cannot go through the barrel of the detector because of their large rapidity values, a rapidity cut was applied (η < 1.25) and it was observed that the unexpected sudden drop around 3 GeV is still there after the application of the cut (Figure 5.7).
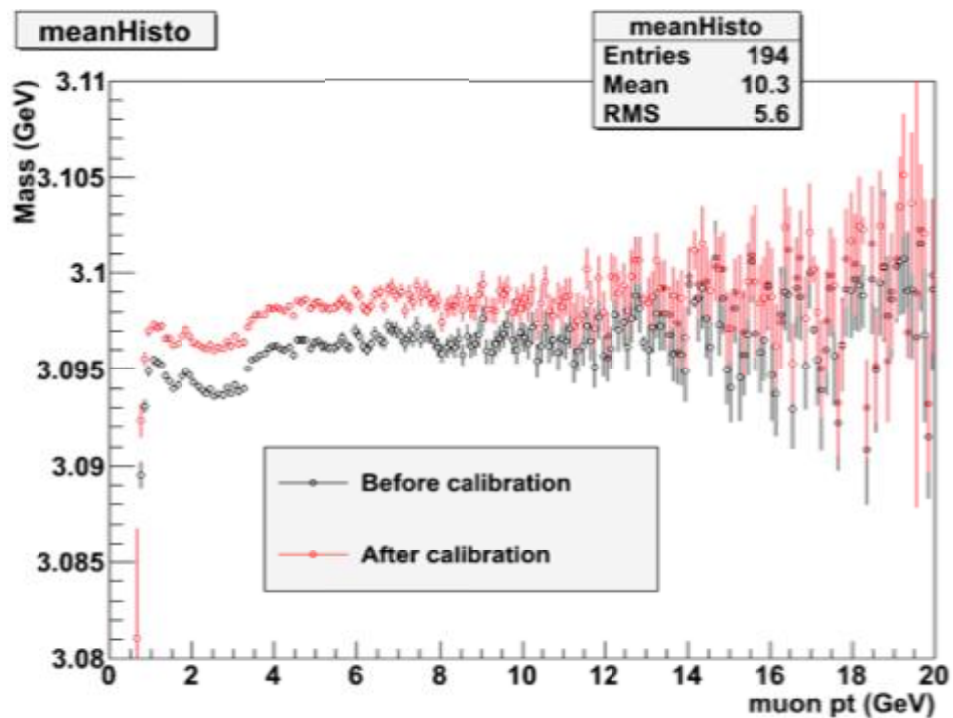
Figure 5.7. The mass versus momentum graph of muon pairs for the 2011 MonteCarlo with the cut J/ψ pseudorapidity < 1.25

The next step was the investigation of the mass resolutions of the muon pairs as a function of the eta of the muons and the Figure 5.8 and 5.9 were obtained. The green line shows reco-gen derived resolution (true resolution), The red lines show the mass resolution before and the blue lines after the fit.
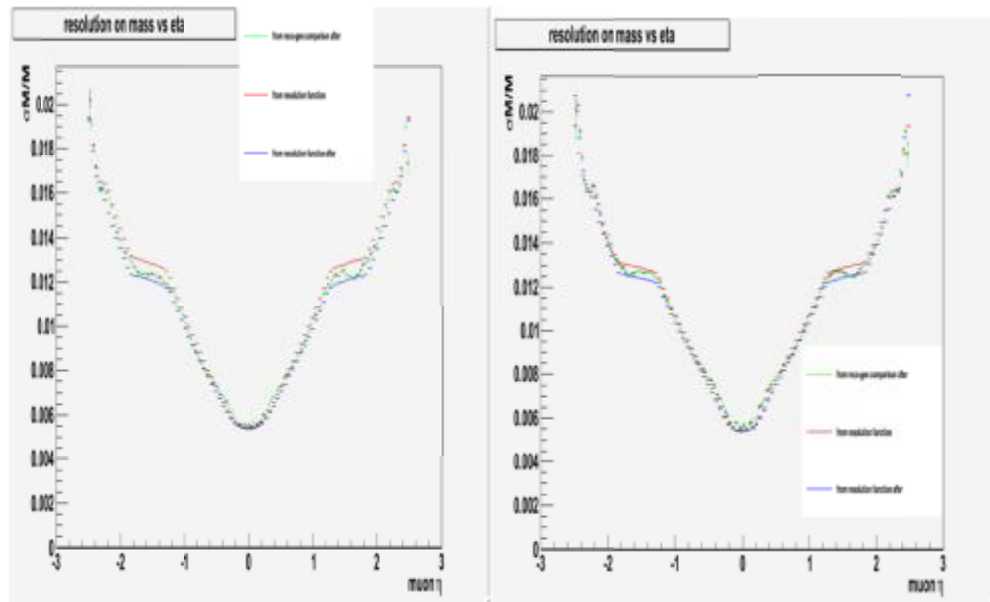
Figure 5.8. The plots of the mass resolutions of di-muons versus η of muons for the old MC (left) and for new MC (right).
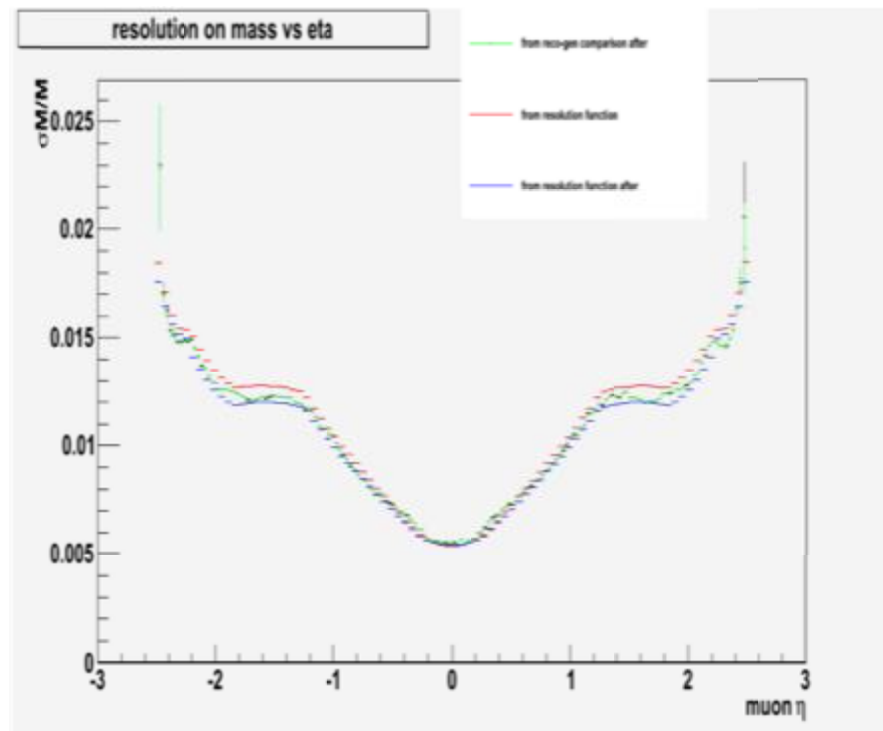
Figure 5.9. The plots of the mass resolutions of di-muons versus η of muons for the new MC after rapidity cut

These plots are showing that the applied fit works and mass resolution values approach the expected values.

The same steps were repeated for the momentum resolutions of the muon pairs (Figure 5.10 and Figure 5.11).
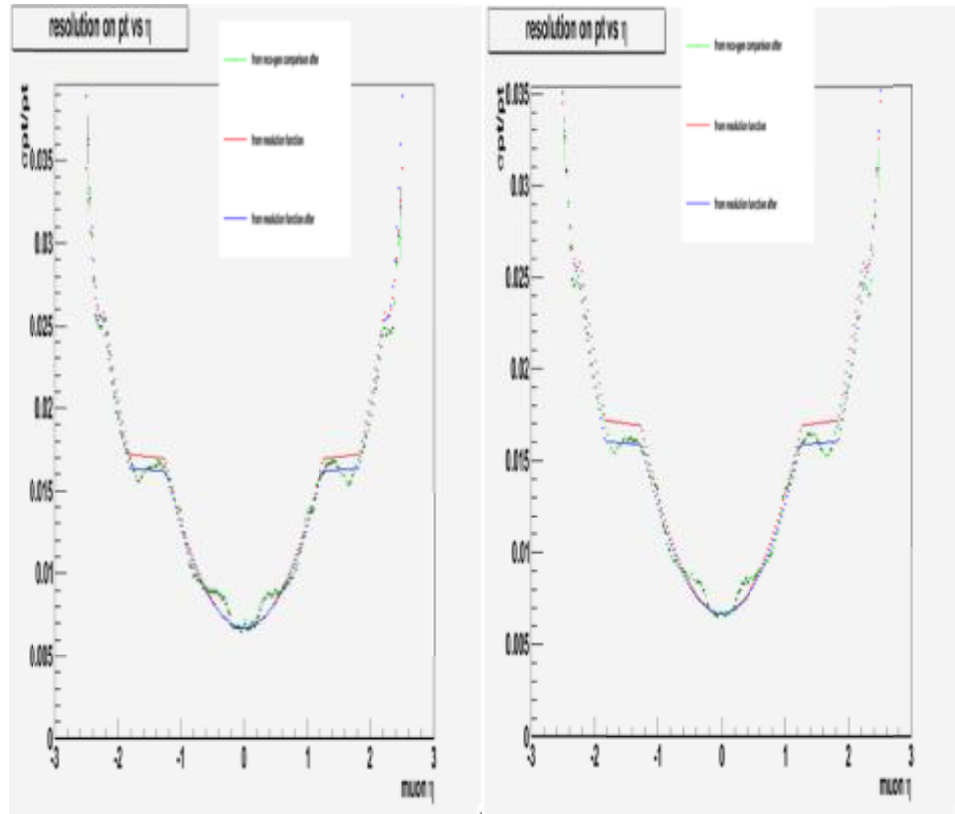
Figure 5.10. The plots of the momentum resolutions of the di-muons versus ɧ of muons for old MC (left) and new MC (right)
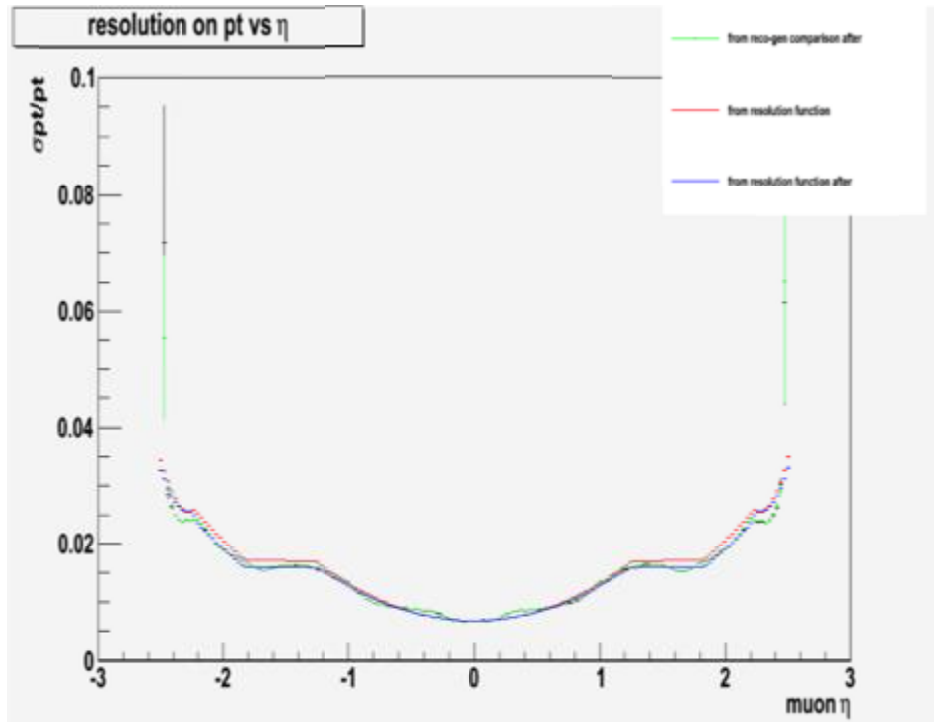
Figure 5.11. The plot of the momentum resolutions of the di-muons versus h of muons for new MC after the pseudorapidity cut

It is also seen from the momentum resolution plots that blue lines which represent the values after the fit, approach the green lines representing the expected values closer than the red lines which represent the values before the fit.

In the next step, the mass resolution plots of the two MC samples were drawn for each muon of a muon pair versus muon momenta (Figure 5.12 and Figure 5.13).
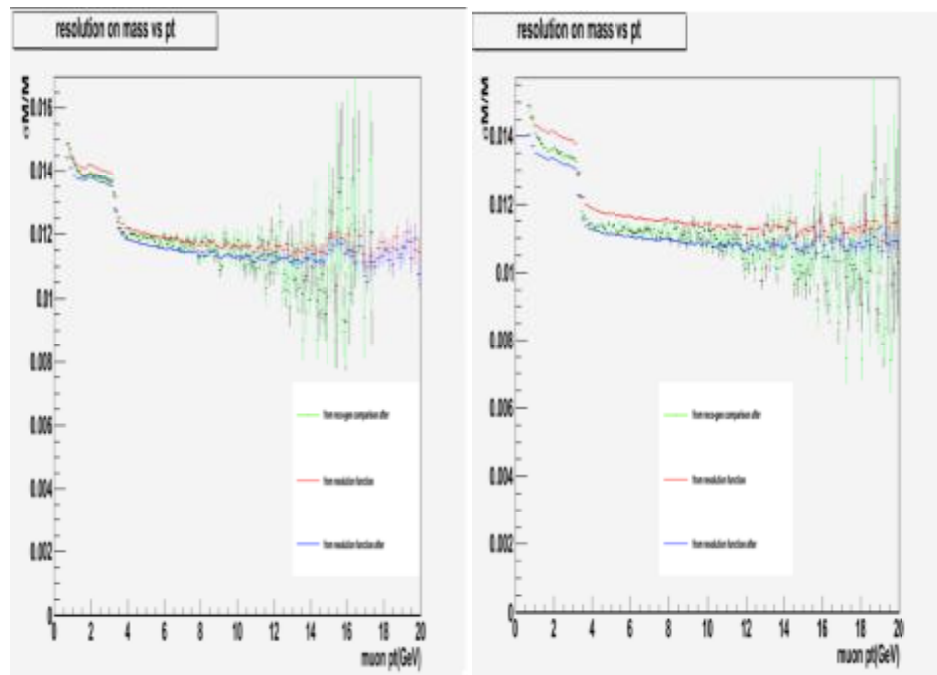
Figure 5.12. The plots of mass resolution versus momentum of the muon pairs for old MC (left) and new MC (right)
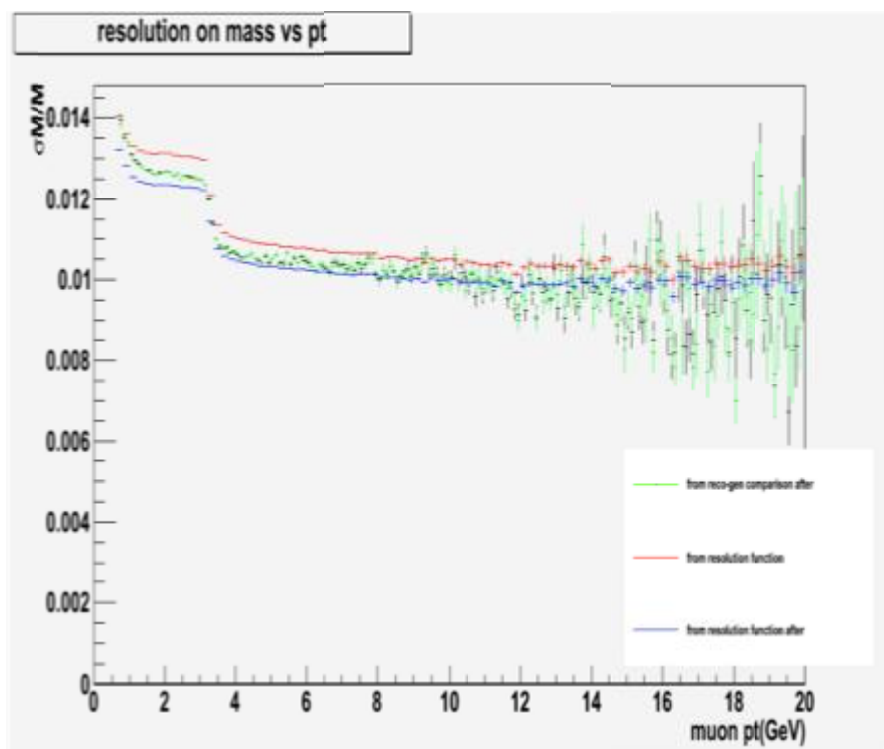
Figure 5.13. The plots of mass resolution versus momentum of the muon pairs for new MC after rapidity cut

After using MuScleFit algorithm in these MC samples, new MC sample which was produced in 2011 is agreed to be used.

5.6. Results on Data and Simulation

Muon Scale Fit results on data and simulation are shown in Figures 5.14 and 5.15. The fit is unbinned. The fitted distributions show good agreement for all η bins.
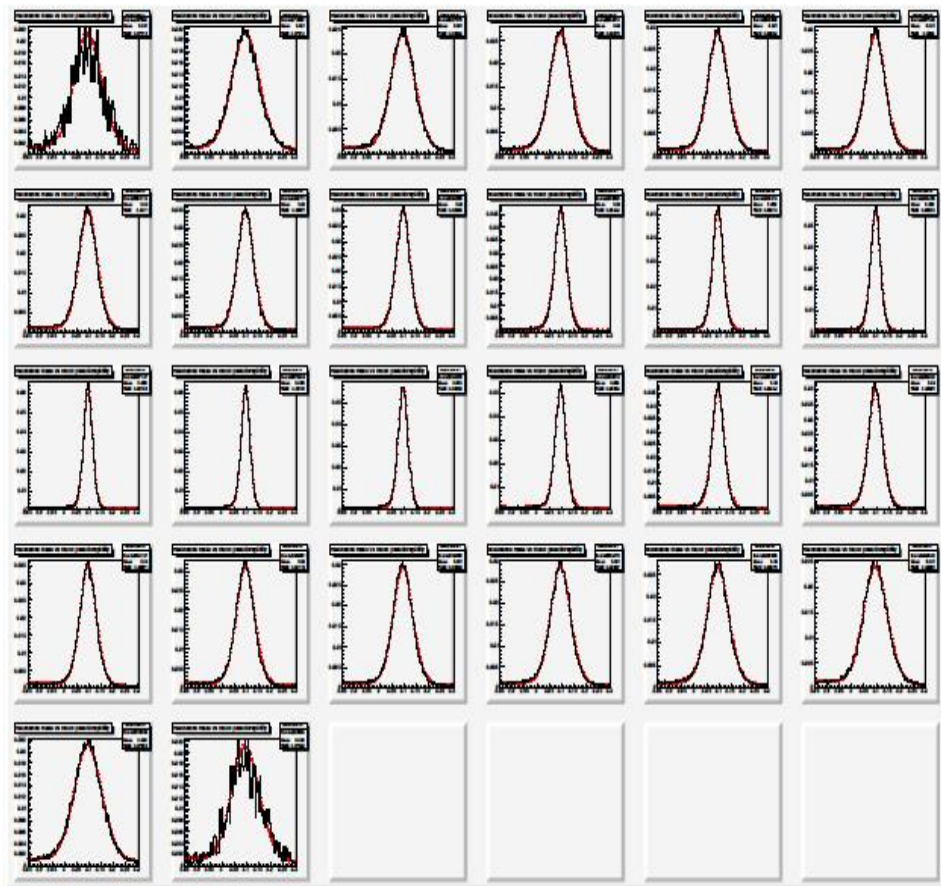
Figure 5.14. Data fit results. The projections in bins of the muons η (filled for both muons) of the mass distribution and the probability distribution function
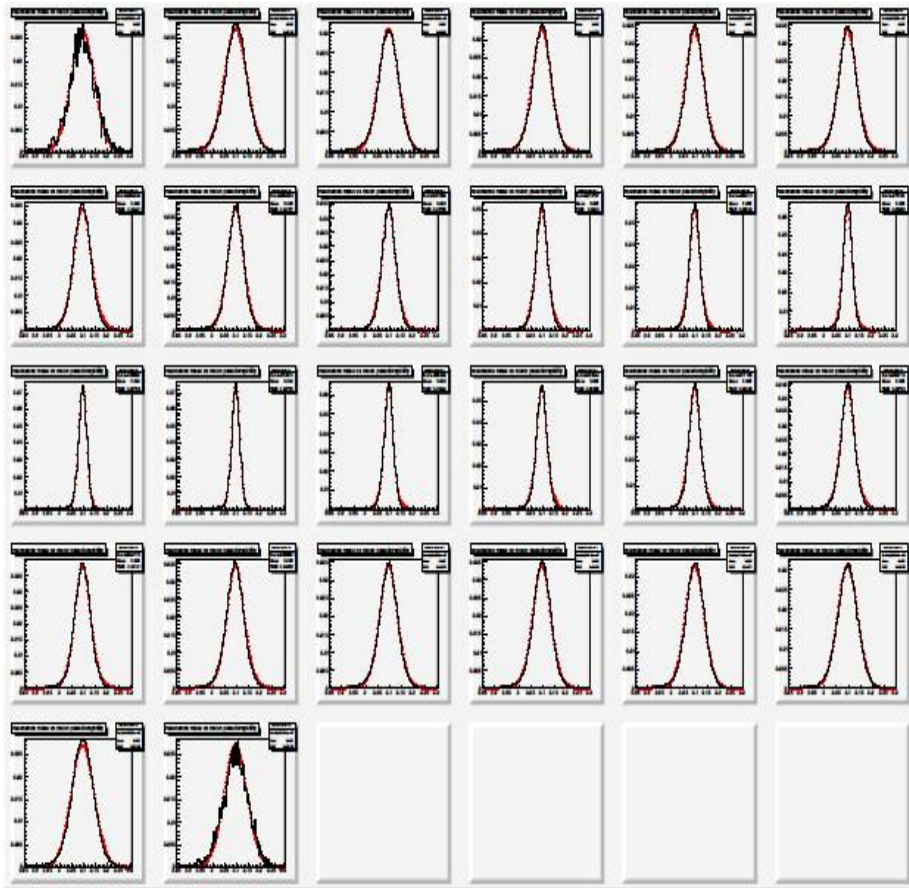
Figure 5.15. MC fit results

The parameters for the scale functions are given in Table 5.2 for Data and 5.3 for MC.

Table 5.2. Scale Fit Parameters for Data

Scale Fit Parameters	
parameter 1	1.000570 ± 0.000017
parameter 2	$(10.8 \pm 2.4) \ 10^{-04}$
parameter 3	$-(2 \pm 3) \ 10^{-03}$
parameter 4	$-(3 \pm 4) \ 10^{-03}$
parameter 5	1.563 ± 0.042
parameter 6	0 (fixed)
parameter 7	$(205.0 \pm 7.7) \ 10^{-06}$
parameter 8	6 (fixed)

Table 5.3. Scale Fit Parameters for MC

Scale Fit Parameters	
parameter 1	0.999777 ± 0.000015
parameter 2	$(-39.6 \pm 6.3) \, 10^{-05}$
parameter 3	$(44.2 \pm 2.3) \, 10^{-04}$
parameter 4	$(3 \pm 6) \, 10^{-04}$
parameter 5	(1.69999 ± 0.00024)
parameter 6	0 (fixed)
parameter 7	$(98.4 \pm 2.0) \, 10^{-06}$
parameter 8	6 (fixed)

The distribution of the peak from the CB fit as a function of η for data and MC is shown in Figure 5.16 for positive charged muons and in Figure 5.17 for negative charged muons. The high eta regions are corrected after the calibration. A shift by 0.1% is observed for both negative and positive charged muons.

Improvement in the distribution is observed at low p_T regions for both data and MC as shown in the Figure 5.18, there is an overall shift in data and the fit did not work very well for very low p_T (<2 GeV).
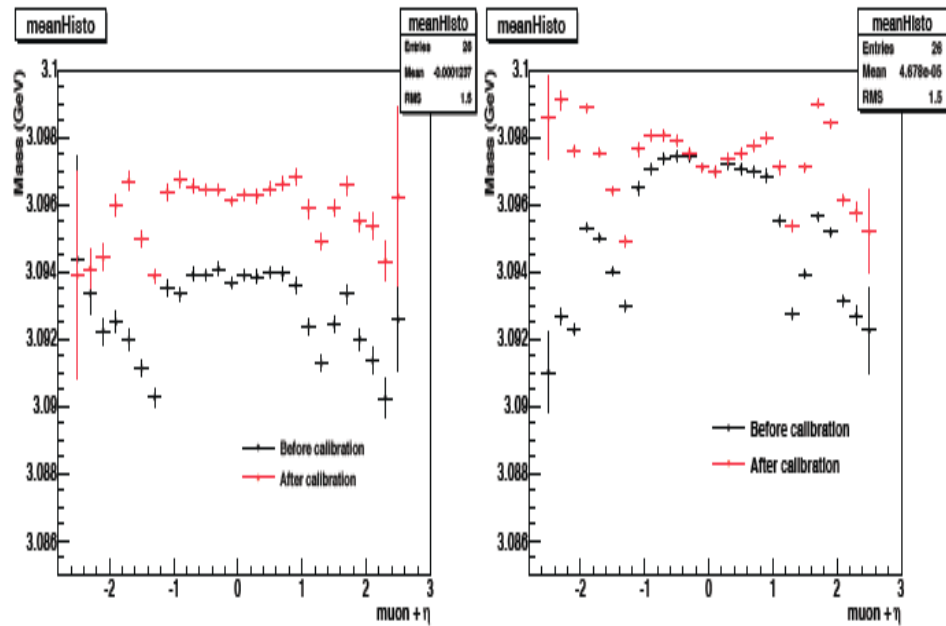
Figure 5.16. Results of the mass correction vs positive charged muons η before (black) and after (red) the calibration procedure on Data (left) and simulation (right)
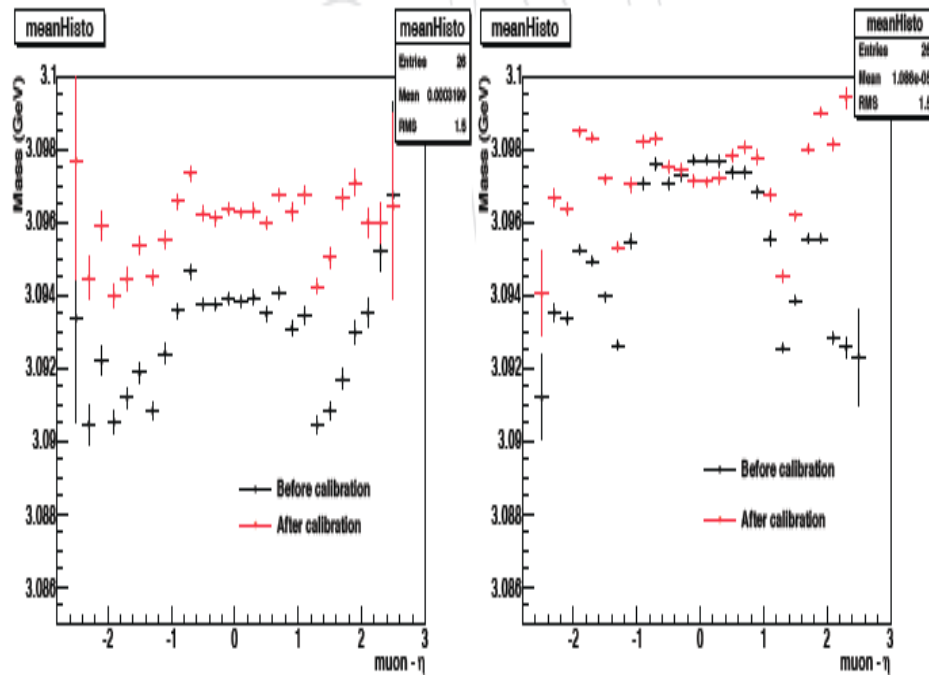
Figure 5.17. Results of the mass correction vs negative charged muons η before
             (black) and after (red) the calibration procedure on Data (left) and
             simulation (right)

For the resolution on single muon p_T, the simulation fit agrees well with the
MC truth. Data and MC show a good agreement in the barrel region whereas data
resolution is slightly worse in the endcaps.
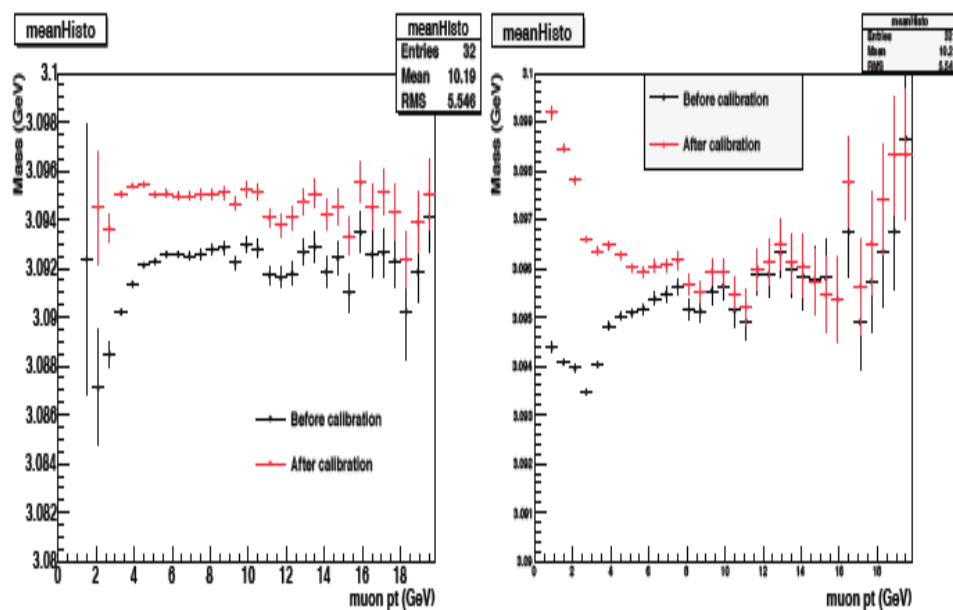
Figure 5.18. Results of the mass vs muon p_T before (black) and after (red) the calibration procedure on Data (left) and simulation (right). Plot filled for both muons
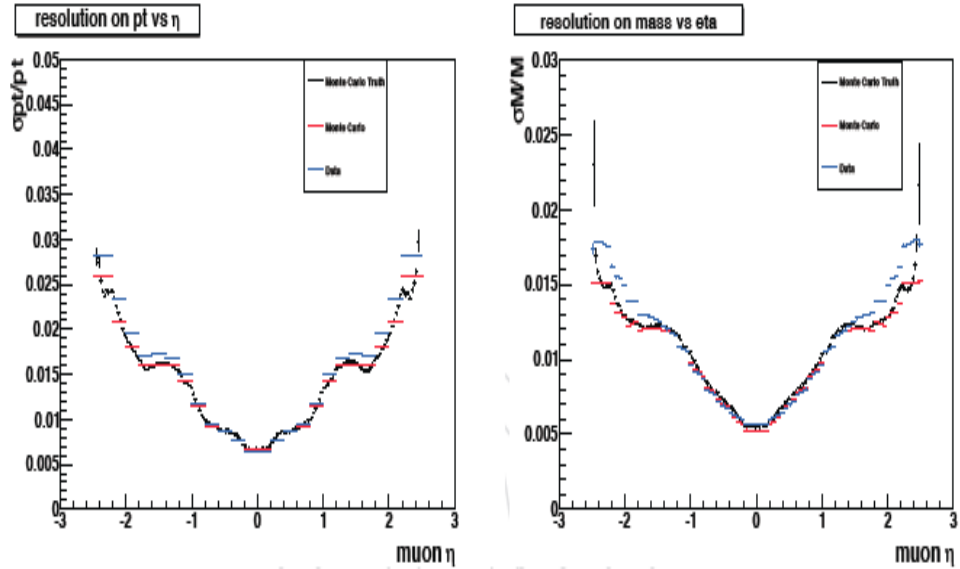
Figure 5.19. Results of the resolution on single muon p_T vs muons h (left). Mass resolution vs muons h (right). Black, blue and red colors are refer to MC truth, data and MC respectively

Simulation Fit agrees well with the MC truth. Data and MC show a good agreement in the barrel. Data resolution is slightly worse in the endcaps (see Figure 5.19).

p_T resolution is extracted from mass resolution neglecting correlations. As shown in Figure 5.20 the agreement of the mass resolution with MC truth shows that these assumptions are good.
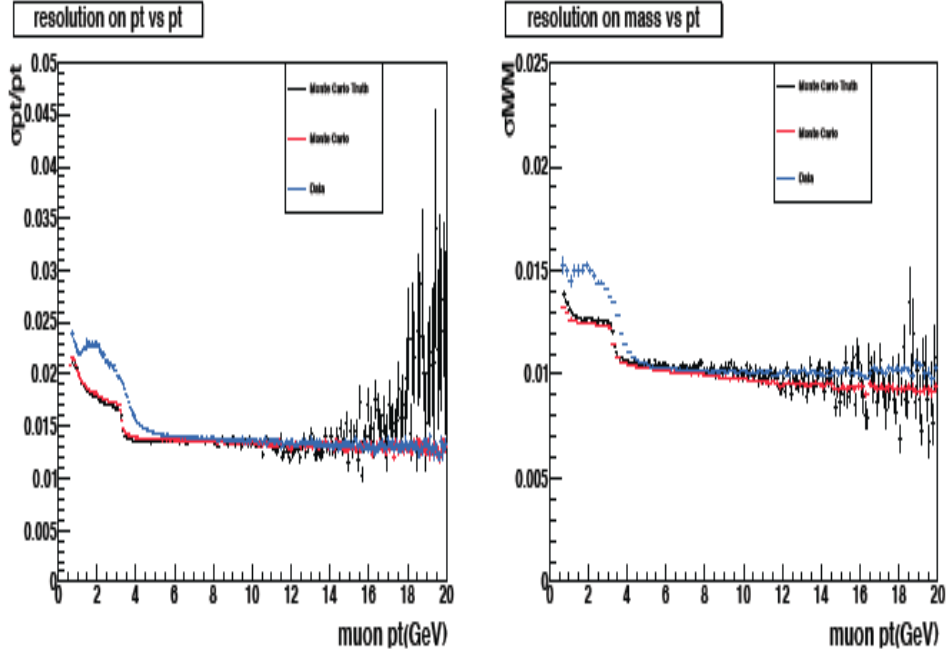
Figure 5.20. Results of the resolution on p_T vs p_T (left). Mass resolution vs p_T (right). Black, blue and red colors refer to MC truth, data and MC respectively

5.7. Comparison with 2010 Data

When 2010 and 2011 scale correction on data compared, the overall effect is 0.1% in both cases as shown in Figure 5.21. This is what we expected because the accuracy of the measured p_T of a track depends on the accuracy of the hit position and this depends on how well the alignment of the tracker is known, how well the material effects are accounted for and so on. The difference between 2010 and 2011 data are due to increased pile up in 2011 and different triggers that were used. The presence of additional tracks' interactions (pile-up) in the same event will not affect the track measurement unless the hits of different tracks overlap (at least partially). The tracker granularity is good enough to cope with the 2011 pile-up without causing this problem. Therefore no effect of pile up is expected on momentum scale or resolution.

Not an appreciable effect is expected because of the changing triggers either, because the trigger can shape the mass distribution, but this should be a second order effect. The results obtained in this study is in agreement with these expectations and show that this method is independent of changing pile up and trigger.
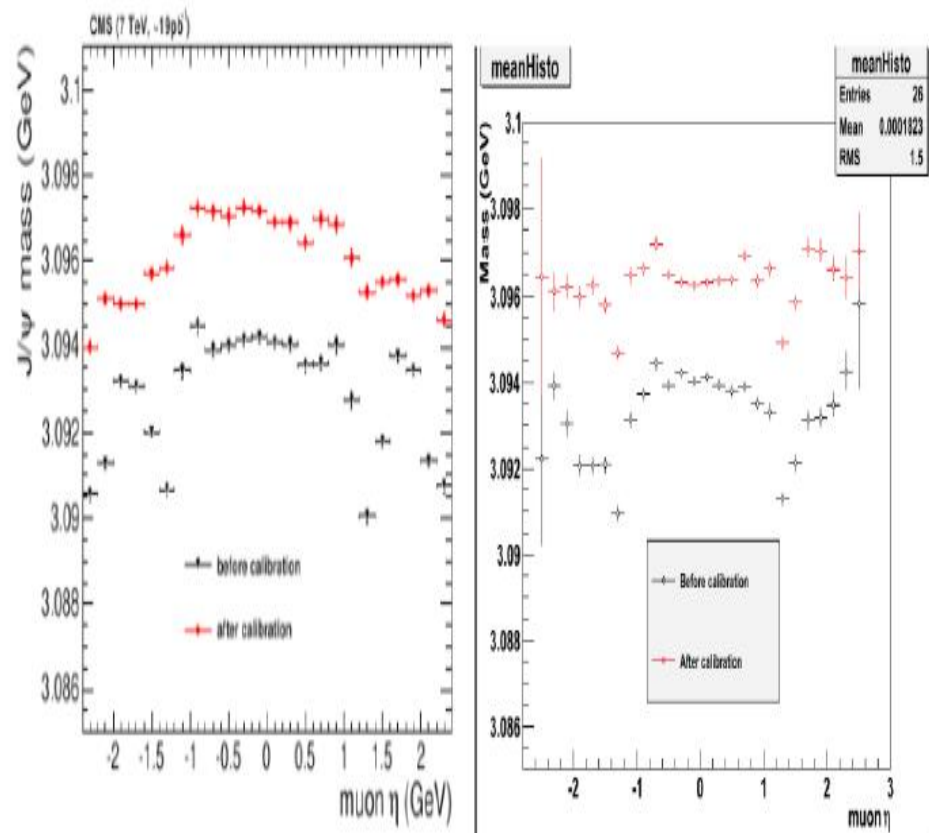
Figure 5.21. Comparison of 2010 (left) and 2011 (right) scale corrections on data

6. CONCLUSION

This thesis comprises of two sections, Installation and Commissioning work done for the HCAL is written in Chapter 4 and MuScleFit analysis is written in Chapter 5. All the work presented in this thesis were performed for the CMS experiment at CERN.

The Installation and Commisioning work consists of two sub-sections: Light Emitting Diode (LED) Stability of the HB and HE Detectors and HB HE Energy Reconstruction. In the first sub-section the shifts in specific channels of HB and HE sub detectors were eliminated by using a normalization method. The channels which have RMS/Mean LED signal values were over than expected and bad runs with bad fractional signal change values even after this normalization procedure are determined. These runs are extracted from future analysis. In the second sub-section HB HE Energy Reconstruction was investigated for 2TS and 4TS Reco samples and different phase settings. In order to minimize the effects of pile up it was decided that 2TS RECO samples should be used instead of 4TS RECO samples and phase setting should be taken as +4 ns.

In Chapter 5 MuScleFit Analysis is explained in detail. In this analysis $J/\psi \rightarrow \mu\mu$ events collected at 2011 data taking are used to investigate the mass and momentum resolution. Biases in the muon-momentum scale are found and a suitable function is used to correct them. An overall shift of 0.1% is observed. The deviation increases only at very low momentum ($p_T < 6$ GeV) and high pseudorapidity. The resolution in data appears to be in good agreement with the simulation in the barrel while it is slightly worse at high pseudorapidity.

As can be seen from the name of the experiment, Compact Muon Solenoid, accurate muon measurement is crucial and therefore the results of the J/ψ momentum scale and resolution measurement obtained in this thesis are used to estimate the systematic errors due to momentum scale and resolution in all analyses dealing with low p_T muons in CMS experiment at CERN.

REFERENCES

AALTONEN, T. (CDF and DØ Collaborations) (2010). "Combination of Tevatron searches for the standard model Higgs boson in the W^+W^- decay mode". Physical Review Letters 104 (6): 61802.

ACHARYA, B. S. et all 2006 "The CMS Outer Hadron Calorimeter" CMS Note 2006/127 (http://cds.cern.ch/record/973131/files/NOTE2006_127.pdf)

ATLAS Collaboration (2012). "Observation of a New Particle in the Search for the Standard Model Higgs Boson with the ATLAS Detector at the LHC". Physics Letters B 716 (1): 1–29.

BOLOGNESI, S. BORGIA, M. A. CASTELLO, R. MARIOTTI, C. DE MATTIA, M. DORIGO, T. 2010 "Calibration of track momentum using di-muon resonances in CMS" (http://cms.cern.ch/iCMS/jsp/openfile.jsp?tp=draft&files=AN2010_059_v1.pdf)

BONTENACKELS, M. 2005 CMS CR 2005/020 "The CMS Muon Spectrometer" CMS CR 2005/020 (http://cds.cern.ch/record/886223/files/cr05_020.pdf)

CDF Collaboration, the D0 Collaboration, the Tevatron New Physics, Higgs Working Group. (2012) "Updated Combination of CDF and D0 Searches for Standard Model Higgs Boson Production with up to 10.0 fb-1 of Data" arXiv: 1207.0449

CMS Collaboration 1997 "The Muon Project, Technical Design Report",

CERN/LHCC 97-32, CMS TDR 3, (https://cdsweb.cern.ch/record/343814)

CMS Collaboration 1997 "The Electromagnetic Calorimeter Technical Design Report", CERN/ LHCC 97-33 CMS TDR 4, http://cds.cern.ch/record/349375/files/ECAL_TDR.pdf

CMS Collaboration (2000) "Addendum to the CMS Tracker TDR", CERN/LHCC 2000-016; CMS TDR 5 Addendum 1.

CMS Collaboration (2006) "CMS Physics: Technical Design Report Volume 1: Detector Performance and Software", CERN/LHCC 2006-001; CMS TDR 8.1.

CMS Collaboration (2007) "CMS Physics: Technical Design Report Volume 2: Physics Performance", CERN/LHCC 2006-021; CMS TDR 8.2.

CMS Collaboration (2008), "The CMS Experiment at the CERN LHC", JINST 3 S08004.

CMS Collaboration (2012) "Observation of a new boson at a mass of 125 GeV with the CMS experiment at the LHC", Physics Letters B 716 (1): 30–61.

ENGLERT, F. and BROUT, R. 1964 Physical Review Letters, 13, 321

FOCARDI, E., 2011. "Status of the CMS detector", Conference Report, CMS CR-2011/214, TIPP 2011, http://cds.cern.ch/record/1395445/files/CR2011_214.pdf

GUNION, J.F. etal.(1990) The Higgs Hunter's Guide, Addison-Wesley, Redwood City, CA.

HIGGS, P. W. 1964 Physics Letters, 12, 132; Physical Review Letters, 13, 508

LEIKE, A. (1999) "The phenomenology of extra neutral gauge bosons", Phys. Rept 317 143-250.

SPEER, T., PROKOFIEV, K., FRUHWIRTH, R., WALTENBERGER, W. AND VANLEAR, R. 2006 "Vertex Fitting in the CMS Tracker". CMS NOTE-2006/032, YAO, W. M. (2006). Searches for Higgs Bosons, "Review of Particle Physics" Journal of Physics G 33: 1

https://twiki.cern.ch/twiki/bin/view/CMSPublic/SWGuideStandAloneMuonReco

http://en.wikipedia.org/wiki/Crystal_Ball_function

http://en.wikipedia.org/wiki/Quark#mediaviewer/File:Standard_Model_of_Elementary_Particles.svg

http://www.lhc-closer.es/1/3/4/0

http://cms.web.cern.ch/news/cms-detector-design)

http://www.hephy.at/user/friedl/diss/html/node27.html

http://arxiv.org/pdf/0810.4133.pdf

RESUME

She was born in Adana in 1985. She graduated from primary school in Lefkoşe, Cyprus. She then went back to Adana and completed her secondary school and high school degrees. She enrolled in the physics department of Çukurova University in 2002 and graduated in 2006. She continued to study for her PhD in High Energy Physics at the Institude of Natural and Applied Sciences in Çukurova University where she is still enrolled.

APPENDIX

A. TABLES OF CHANNELS WITH RELATIVE RMS > 0.05

Table A.1. Channels with relative RMS value greater than 0.05 for HE

Eta,phi,depth	RMS/Mean
25,3,2	0.274
18,4,1	0.323
18,4,2	0.325
20,4,1	0.325
24,5,1	0.328
28,5,1	0.328
- 29,11,2	0.327
- 25,11,1	0.320
25,17,2	0.324
27,17,3	0.323
- 27,19,3	0.326
- 29,23,2	0.053
- 23,23,1	0.058
- 23,23,2	0.061
- 20,24,1	0.051
- 19,24,1	0.053
- 19,24,2	0.073
- 18,24,2	0.050
27,31,2	0.196
18,32,1	0.328
18,32,2	0.326
19,32,2	0.329
20,32,1	0.329
-20,33,1	0.325
16,40,3	0.326
28,43,1	0.055
- 22,45,2	0.327
- 21,45,2	0.322
- 20,45,1	0.317
- 19,45,2	0.324
- 19,46,1	0.129

26,53,1	0.329
21,59,2	0.075
23,59,1	0.075
23,59,2	0.076
25,59,1	0.076
25,59,2	0.075
27,59,1	0.076
27,59,2	0.076
27,59,3	0.076
29,59,2	0.076
16,60,3	0.075
17,60,1	0.075
18,60,1	0.077
18,60,2	0.075
19,60,1	0.076
19,60,2	0.074
20,60,2	0.075

Table A.2. Channels with Relative RMS value greater than 0.05 for HE after normalization

Eta,phi,depth	RMS/Mean
18,4,2	0.060
24,5,1	0.070
28,5,1	0.068
- 25,11,1	0.054
25,17,2	0.061
27,17,3	0.081
- 29,23,2	0.052
- 23,23,1	0.058
- 23,23,2	0.060
- 19,24,1	0.051
- 19,24,2	0.073
- 18,24,2	0.051
- 23,23,1	0.058
- 23,23,2	0.061
- 19,24,1	0.051

- 19,24,2	0.073
- 18,24,2	0.051
27,31,2	0.066
18,32,1	0.052
19,32,2	0.097
20,32,1	0.067
- 21,45,2	0.135
- 20,45,1	0.237
- 19,45,2	0.068
21,59,2	0.073
23,59,1	0.073
23,59,2	0.073
25,59,1	0.074
25,59,2	0.074
27,59,1	0.073
27,59,2	0.073
27,59,3	0.073
29,59,2	0.073
16,60,3	0.074
17,60,1	0.074
18,60,1	0.073
18,60,2	0.075
19,60,1	0.073
19,60,2	0.074
20,60,2	0.074

B. CRYSTAL BALL FUNCTION

The Crystal Ball function is a probability density function used to model lossy processes in high-energy physics. It has a Gaussian core portion and a power-law low-end tail, below a certain threshold. Both the function itself and its first derivative are continuous. The Crystal Ball function is given by:

$$f(x; \alpha, n, \bar{x}, \sigma) = N \cdot \begin{cases} \exp(-\frac{(x-\bar{x}^2)}{2\alpha^2}), \ for \ \frac{x-\bar{x}}{\sigma} > -\alpha \\ A \cdot (B - \frac{x-\bar{x}}{\sigma})^{-n}, \ for \ \frac{x-\bar{x}}{\sigma} \ x \leq -\alpha \end{cases}$$

where:

$$A = (\frac{n}{|\alpha|})^n \cdot \exp\left(-\frac{|\alpha|^2}{2}\right),$$

$$B = \frac{n}{|\alpha|} - |\alpha|,$$

$$N = \frac{1}{\alpha(C+D)}$$

$$C = \frac{n}{\alpha} \cdot \frac{1}{n-1} \cdot \exp\left(-\frac{|\alpha|^2}{2}\right)$$

$$D = \sqrt{\frac{\pi}{2}} \ (1 + \text{erf} \left(\frac{|\alpha|}{\sqrt{2}}\right)$$

N (Skwarnicki 1986) is a normalization factor, α, *n*, $\bar{x}$, σ are fitted parameters with the data and erf is the error function. (http://en.wikipedia.org/wiki/Crystal_Ball_function)
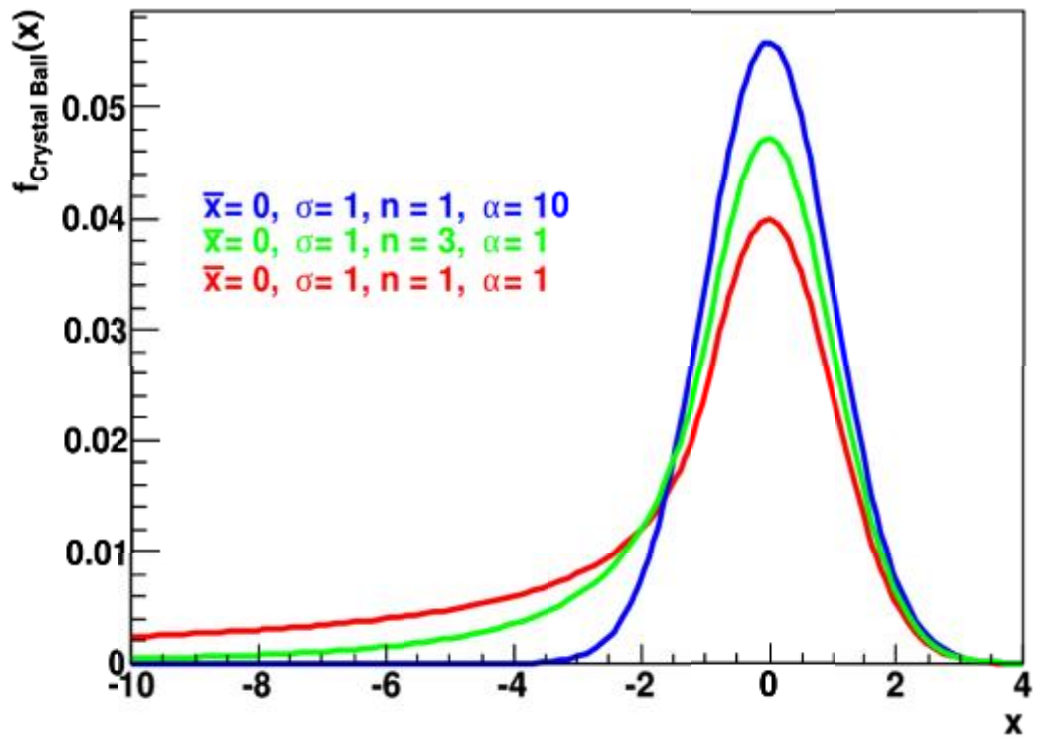
Figure B.1. Examples of the Crystal Ball Function
(http://en.wikipedia.org/wiki/Crystal_Ball_functio